NTNU – Trondheim
Norwegian University of
Science and Technology

Spinel oxide protective coatings for solid oxide fuel cell interconnects

Thong Xuan Nguyen

Materials Science and Engineering
Submission date: July 2013
Supervisor: Hilde Lea Lein, IMTE
Co-supervisor: Mari-Ann Einarsrud, IMT
Sophie Weber, IMT

Norwegian University of Science and Technology
Department of Materials Science and Engineering

Preface

This master thesis has been written as part of the course TMT 4900 and carried out at the Department of Materials Science and Engineering, Norwegian University of Science and Technology (NTNU).

Associate Professor Hilde Lea Lein has been the main supervisor, while Professor Mari-Ann Einarsrud and Post doc. Sophie Weber has been co-supervisors. Ph.D. candidate Stefanus Lumban Tobing has also been involved in this work. The above mentioned are all associated with NTNU.

Acknowledgements

I would like to express my gratitude to my supervisor Assoc. Prof. Hilde Lea Lein for her good advices, guidance and support throughout this thesis. I would also thank co-supervisors Prof. Mari-Ann Einarsrud and Post doc. Sophie Weber for their knowledge and encouragement. In addition, Weber, and Ph.D. candidate Stefanus Lumban Tobing has been of great help for guiding me through experimental procedures and sharing their experiences with me.

My gratitude also goes to the administrative and technical staff of the department who has handled all paperwork very efficiently and provided me with necessary equipment training.

Finally, I would like to thank my family. Their belief in me, has laid the foundation for my five years of study at NTNU, culminating in this master thesis.

Thong Xuan Nguyen

Trondheim, 2nd July 2013

Summary

Metallic interconnects in solid oxide fuel cells are dependent on protective coatings to ensure adequate application lifetime. Of the many coatings investigated, spinel composition coatings display the most promising results. Currently, these coatings are deposited by expensive powder based methods. In contrast, spray pyrolysis is a deposition technique that is regarded as both simple and cost-effective. Thus it appears as an attractive alternative, but has until recently been given little attention.

In this work, spinel manganese cobalt oxide ($MnCo_2O_4$) coatings deposited by spray pyrolysis has been studied. The influence of substrate surface roughness was evaluated and it was found that substrates with a higher degree of surface finish yielded the best coatings with respect to microstructure.

Furthermore, the layer-by-layer approach was employed in order to produce thicker coatings. This proved successful as stable multilayer coatings with increased thickness were obtained, although the desired thickness value of 10 µm was not reached in this work.

Various heat treatments were conducted in order to elucidate their effect on the coating density, crack evolution and overall coating microstructure. Findings show that longer heat treatments at elevated temperatures resulted in denser coatings. However, the heating temperature must be kept on a reasonable level where phase pure $MnCo_2O_4$ is maintained. For heat treatment in air, 800 °C is close to the maximum temperature limit that can be used. For heat treatment in argon, a temperature of 1100 °C proved to exceed the phase stability region of pure $MnCo_2O_4$. A subsequent heat treatment at lower temperature proved futile to recover a phase pure coating.

Sammendrag

Metalliske koblingsplater i fastoksid-brenselsceller er avhengig av beskyttende belegg for å oppnå en tilfredsstillende brukslevetid. Av flere undersøkte belegg, utmerker belegg av spineller seg som spesielt lovende. I dag blir disse beleggene produsert ved bruk av dyre pulverbaserte metoder. Til sammenligning er spray pyrolyse en deponeringsteknikk som regnes for å være både enkel og kostnadseffektiv. Dermed går det for å være et attraktivt alternativ. Likevel har ikke metoden fått noe særlig med oppmerksomhet før inntil nylig.

I dette arbeidet har belegg av spinellen mangan kobolt oksid ($MnCo_2O_4$), produsert ved spray pyrolyse, blitt undersøkt. Påvirkningen av overflateruheten til substratet ble avdekket og det ble funnet ut at substrater med høyere grad av polering gav de beste beleggene med hensyn på mikrostruktur.

Lag-for-lag deponering ble brukt som framgangsmåte for å produsere tykkere belegg. Dette viste seg å være en effektiv metode ettersom stabile flersjiktsbelegg med økt tykkelse ble oppnådd, til tross for at den ønskede tykkelsen på 10 µm ikke ble nådd i dette arbeidet.

Ulike varmebehandlinger ble utført for å belyse effekten dette hadde på beleggtettheten, sprekkutvikling, samt den generelle mikrostrukturen. Funn viser at lengre varmebehandling ved høyere temperaturer resulterte i tettere belegg. Imidlertid må behandlingstemperaturen holdes på et forsvarlig nivå hvor faserenheten til $MnCo_2O_4$ opprettholdes. For varmebehandlinger i luft viste det seg at 800 °C er nær maksimumstemperaturen som kan brukes. Vedrørende varmebehandling i argon viste det seg at 1100 °C overskred maksimumstemperaturen for stabilitetsregionen for ren $MnCo_2O_4$. Det var siden ikke mulig å gjenopprette et faserent belegg ved påfølgende varmebehandling ved lavere temperatur.

Contents

1 Background

Since the public debate about global climate change became a household topic a mere decade ago, our society has experienced an increasing demand for clean energy and power production. Solid oxide fuel cells (SOFCs) represent a promising technology that has the potential to fulfill these requirements, but have yet to be successfully commercialized [1]. A factor that delays the commercialization of the technology is related to the cost and manufacture of suitable interconnect materials.

Interconnects are a vital component of SOFCs as their function is to accumulate a useful voltage by connecting multiple cells in electrical series in a planar SOFC stack. They also act as separator plates, physically separating the anode side and cathode side of two adjoining cells as shown in Figure 1.1. Ceramic materials e.g. lanthanum chromite, were typically used for this purpose until recent advances in SOFC technology lowered the operating temperatures to 650-800 °C. This has allowed the entry of metals and alloys as interconnect materials. Compared to their ceramic counterparts, metallic interconnects offer several advantages, but more importantly is the easy manufacture at lower costs [2, 3].

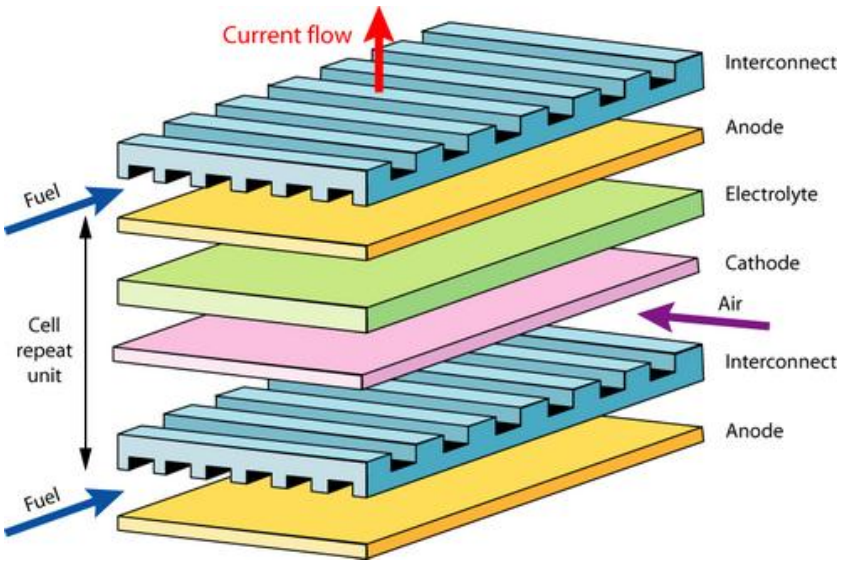

Figure 1.1: Schematic of a SOFC stack [4].

Nowadays, ferritic stainless steels (FSSs) are the preferred material for metallic interconnect application in SOFCs operating at temperatures between 650-800 °C [5]. Still, this choice of material causes new challenges of which oxide scale growth and chromium poisoning are the most severe. Studies that have been carried out to eliminate these issues, point toward protective coatings as the favored solution [6]. However, the coatings are required to be dense and crack-free in order to mitigate the inward diffusion of oxygen and outward diffusion of chromium [7], which are the cause of oxide growth and chromium poisoning respectively. As a consequence, the thickness is also of

substantial importance as it provides a longer diffusion length for the species in question.

Among the various coatings that have been developed, spinel oxide coatings in particular display promising results. They have good electric conductivity, show excellent capabilities to suppress the volatilization of chromium and are compatible with FSSs [6]. More importantly, there exists a variety of methods for applying the coatings, enabling low-cost application techniques to be used. Such a technique is the spray pyrolysis process which has been shown to produce a variety of coatings [8, 9]. By adjusting the process parameters, thickness, density, cracks and the overall coating morphology, as well properties can be tailored.

1.1 Aim of the work

In a preceding work by the author [10], the spray pyrolysis technique was employed in an attempt to produce thick, dense and crack-free coatings of the spinel oxide compound manganese cobalt oxide, formula $MnCo_2O_4$. Emphasis was then given on the deposition parameters in order to obtain successful coatings and understand the chemistry evolution associated with the deposition process.

This study continues to investigate the utilization of spray pyrolysis to produce coatings of $MnCo_2O_4$ with the desired properties. This time, the main attention is directed towards the influence of substrate surface finish and various heat treatments, as well as coating application by the layer-by-layer approach to reduce cracking defects while increasing the thickness of the coating.

2 Introduction

2.1 Solid oxide fuel cells

Fuel cells are electrochemical devices that convert chemical energy of a fuel into electricity and SOFC are regarded as the most promising of them all. They are highly efficient and generate power with low or no pollution. Also a variety of fuels can be used such as hydrogen, natural gases and even carbon monoxide [1]. In addition, SOFC systems can be scaled to use from small portable systems to large systems for distributed power generation [11].

2.1.1 Operating principle

The SOFC consists of two porous electrodes that are separated by a dense, solid oxide ion conducting electrolyte which is impermeable for other species. The operating principle is displayed in Figure 2.1. On the cathode side, oxygen gas molecules react with electrons provided by an external circuit and form oxide ions. These ions migrate through the electrolyte to the anode where they react with the fuel and liberate electrons in the reaction process. These electrons will flow back toward the cathode through an external circuit thereby generating electricity. In the case of a fuel consisting of hydrogen and carbon monoxide, the byproduct of this process is water and carbon dioxide.

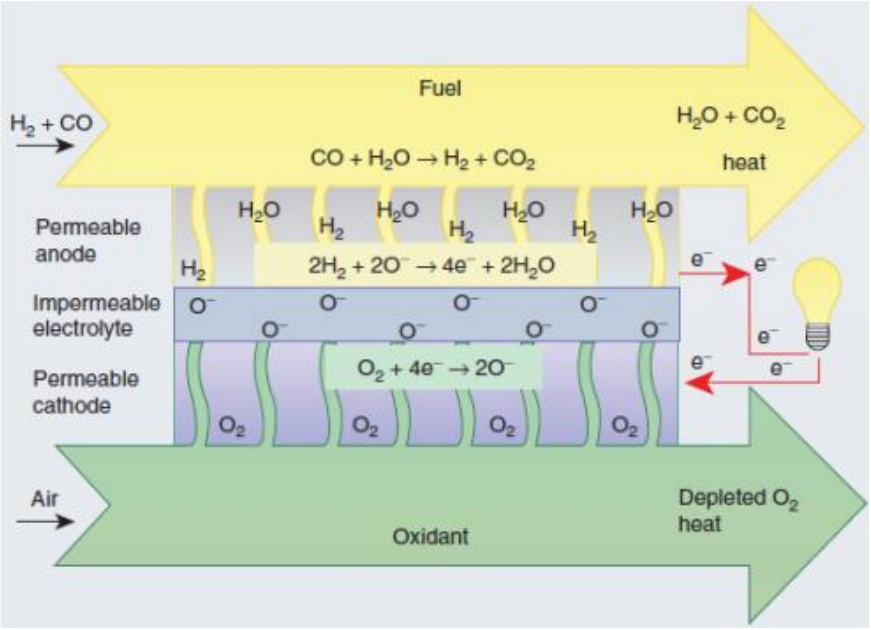

Figure 2.1: Operating principle of a SOFC [11].

As long as both fuel and oxygen are present, electricity is continuously generated. However, the maximum obtainable voltage is limited to 1.1 V for a cell operating at 800 °C with air and room temperature humidified hydrogen as the reaction species [11]. A higher voltage is achieved by the use of interconnects which link the cells in an electrical series.

2.2 Metallic interconnects

For operating temperatures ranging from 650-800 °C, metallic interconnects outcompete their ceramic counterparts in terms of manufacturability and low cost. These are two key factors that promote mass production. They also display higher stability, better electrical and thermal conductivity [3]. However, there are some drawbacks that need to be overcome. In the next sections, a short introduction to metallic interconnects will be provided.

2.2.1 General requirements

The primary function of interconnects is to join the fuel cells in an electrical series and export the current to an external circuit. This implies that any interconnect material must have high electrical conductivity. Oxide layers, which inevitably form on metals under these operating conditions, should therefore also exhibit high levels of conductivity.

Both metal and oxide must be mechanically and chemically stable during operation. This is particularly challenging since the interconnect is exposed to oxidizing and reducing atmospheres at the cathode and anode respectively. Furthermore, the coefficient of thermal expansion (CTE) should be similar to the other cell components and a low permeability of oxygen and hydrogen is necessary. Some mechanical strength is desired as well, in order to maintain the structural integrity of the SOFC system [2, 5, 12].

Table 2.1 present key features of several interesting metallic materials with respect to interconnect requirements. These are all alloys, in which their constituents like Cr, Al and Si, commonly oxidizes at the metal surface to form a scale. As mentioned, this scale must be a good electrical conductor. This is not the case for oxides such as silica (SiO_2) and alumina (Al_2O_3) as they are electrical insulators. In contrast, chromia (Cr_2O_3) show good conductivity with values of 0.02 S/cm at 800 °C. Consequently, alloys containing chrome are the preferred candidates [5].

Table 2.1: Key properties of potential materials for interconnect application. CTE values are valid from room temperature to 800°C [5].

Alloy	**Matrix crystal structure**	**CTE [x 10^{-6} K^{-1}]**	**Oxidation resistance**	**Mech. strength**	**Manufacture**	**Cost**
Cr base alloy	bcc	11.0-12.5	Good	High	Difficult	Very expensive
Ferritic stainless steel	bcc	11.5-14.0	Good	Low	Fairly readily	Less expensive
Austenitic stainless steel	fcc	18.0-20.0	Good	Fairly high	Readily	Less expensive
Fe-Ni-Cr base alloys	fcc	15.0-20.0	Good	High	Readily	Fairly expensive
Ni(-Fe)-Cr base alloys	fcc	14.0-19.0	Good	High	Readily	Expensive

Early attention was given to the Cr base alloys and the FSSs as they both demonstrated a good CTE match with the cell components (10.5-12.5 x 10^{-6} K^{-1}) [3]. Eventually, the Cr base alloys were dismissed due to their difficult manufacturability and high cost, resulting in FSSs as a standalone candidate. Today, FSSs are the most widely studied and utilized alloy group for metallic interconnect applications.

2.2.2 Degradation mechanisms

The use of chromia forming alloys has introduced new challenges related solely to the presence of chromium. Although chromia is a decent electrical conductor, it is still the "bottleneck" in the system as all other components that carry the current possess a higher conductivity [13]. The problem become more prominent as the electrical resistance increases with time since the oxide scale grows thicker during operation. The efficiency of the system will thus decrease.

Chromium poisoning is another problem that can inflict severe damage to the SOFC system and is caused by the volatilization of chromium. Under operating conditions, the chromia scale reacts in the cathodic environment and form volatile chromium species. In dry air, the reaction is as follows:

$$2Cr_2O_3(s) + 3O_2(g) = 4CrO_3(g) \quad (2.1)$$

As a result, CrO_3 becomes the most ample vapor species from the chromia scale. In presence of water vapor, which is typical for a cathodic environment with a relative humidity of 60%, the oxide scale undergoes additional reactions:

$$2Cr_2O_3(s) + 3O_2(g) + 4H_2O(g) = 4CrO_2(OH)_2(g) \quad (2.2)$$

$$Cr_2O_3(s) + O_2(g) + H_2O(g) = CrO_2OH(g) \quad (2.3)$$

At 800 °C, $CrO_2(OH)_2$ has a vapor pressure about two orders of magnitude higher than that of CrO_3, implying a drastic increase in the overall partial pressure of Cr species. Moreover, the reactions are reversible, entailing that both chromium scale formation and volatilization occur for high-temperature oxidation of FSSs [2, 3].

The vaporized Cr species, in particular Cr(VI) species, migrate in the system and to the cathode where they deposit as Cr_2O_3 on the electrode and at the electrode/electrolyte interface. This deposition is simply the reverse of the volatilization and has proven to be detrimental for electrochemical performance of the fuel cell system.

Observations indicate that the chromium poisoning is mitigated by the presence of natural occurring oxide scales on the alloys. For instance, the alloy Crofer 22 APU forms a natural $(Mn,Cr)_3O_4$ spinel scale. The evaporation is still present, but at a lower rate than for pure chromia scales [3]. Nonetheless, the discovery sparked a massive interest in engineered coatings that would prevent chromium poisoning completely and at the same time exhibit better electrical conductivity.

2.3 Coatings

Engineered coatings are widely used in different industries due to their versatility. They are especially utilized in industries where corrosion and wear are main degradation mechanisms. However, coatings can be tailored specifically to any problem based on a broad range of materials such as polymers, metals, ceramics etc. In addition, the selection of coating application techniques is plentiful and coatings of various structure, morphology and properties can be produced.

2.3.1 Requirements for interconnect coatings

For all coating applications, it is vital that the coating adhere to the substrate. Coating adhesion is thus a decisive factor for success. The adhesion is dependent on the bonding forces on the coating/substrate interface. These can be physical, chemical or mechanical (micro- and macro-mechanical) [14, 15]. Thus, it is beneficial that substrate and coating material are similar in terms of crystal structure, thermal expansion, etc. although it is not a necessity. Other general requirements include chemical and mechanical stability as well as relative short application times and low cost.

For the specific case of interconnect coatings, mitigation of high-temperature oxidation and chromium volatilization are the primary goals. This implies that the coating must display a low diffusivity of oxygen and chromium ions. Furthermore, dense and thick coatings, in the range from 10-15 μm, are desired in order to completely isolate the interconnect from the operating environment. Additionally, the protective layer must be an electrical conductor, preferably better than the chromia. A good thermal conductivity and a match in thermal expansion with the surrounding layers are necessary as well [3].

In order to achieve the abovementioned objectives, several coating materials have been elucidated. Among a number of interesting candidates, the spinel manganese cobalt oxide has proven to be particularly promising [6].

2.4 Manganese cobalt oxide

2.4.1 Phase diagram and crystal structure

Manganese cobalt oxide can be formulated as $Mn_{3-x}Co_xO_4$, where Mn_2CoO_4 (x = 1) has a tetragonal spinel structure and $MnCo_2O_4$ (x = 2) possess a cubic spinel structure. These are the two configurations the spinel may appear as. For an intermediate composition, such as $Mn_{1.5}Co_{1.5}O_4$ (x = 1.5), the crystal structure is thus mixed [16, 17]. The stability regions for each of the phases can be seen in the phase diagram displayed in Figure 2.2. The composition of interest in this work, $MnCo_2O_4$, is marked with a blue line in the diagram and is stable for temperatures below 1000 °C.

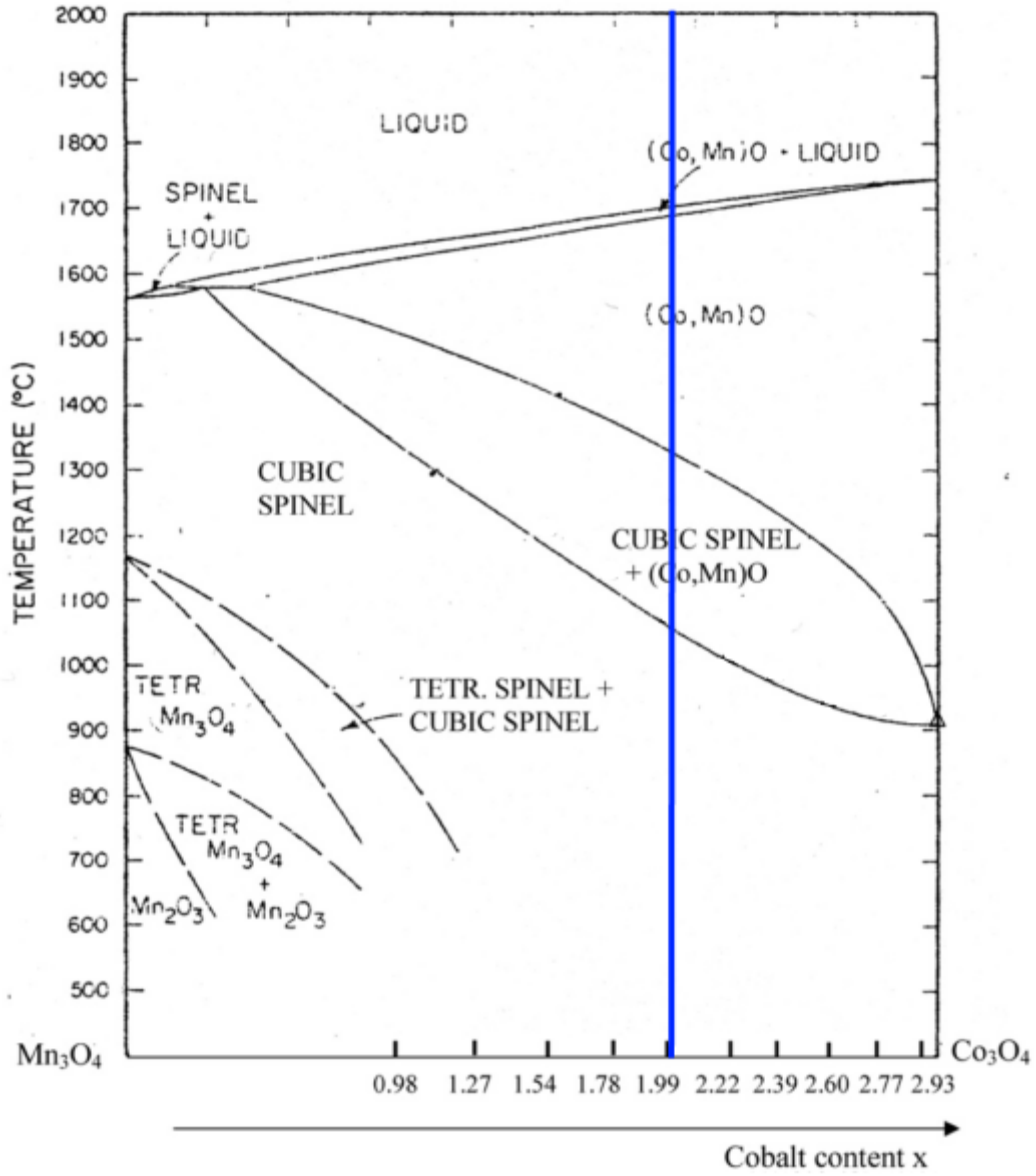

Figure 2.2: Phase diagram of the Mn-Co-O system in air [18].

The unit cell for a cubic spinel is illustrated in Figure 2.3 and contains eight formal units of AB_2O_4. Overall, the cell is comprised of a face centered cubic (fcc) oygen ion lattice. The octahedral sites have an oxygen coordination of six, whereas the tetrahedral sites only have four. For the case of $MnCo_2O_4$, it is a broad agreement that only divalent cobalt ions are situated on the tetrahedral sites [19-21]. Hence, the remaining cobalt and manganese ions occupy the interstitial octahedral sites as Co^{3+} and Mn^{3+} and/or Co^{2+} and Mn^{4+}[16]. As the manganese cations are located on the octahedral sites, $MnCo_2O_4$ is classified as an inverse spinel.

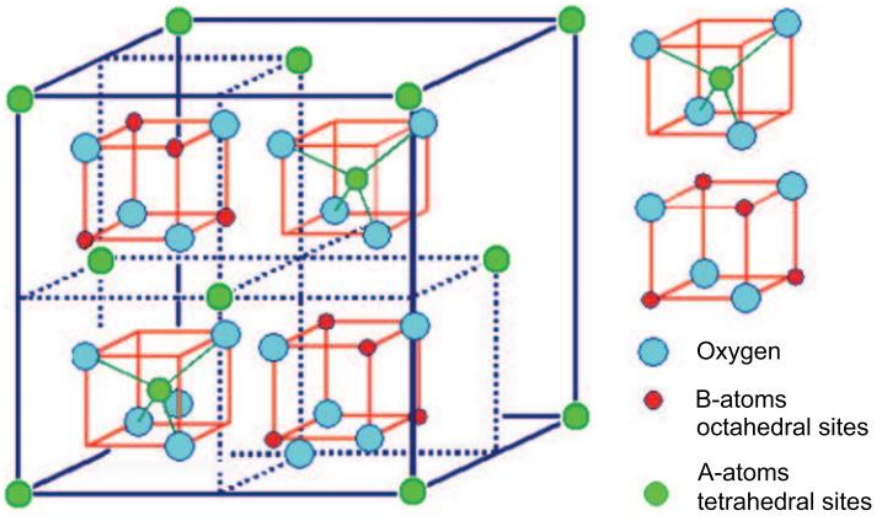

Figure 2.3: Unit cell for a cubic AB_2O_4 spinel. Note that the red cubes are also present in the back half of the cell [22].

2.4.2 Properties of interest

The main reason for the popularity of manganese cobalt oxide coatings is their ability to maintain the mitigation of chromium evaporation even after long term oxidation at operating conditions [23, 24]. Furthermore, the material demonstrates excellent compatibility with FSSs and other components of the cell with respect to thermal expansion behavior as seen on Figure 2.4b.

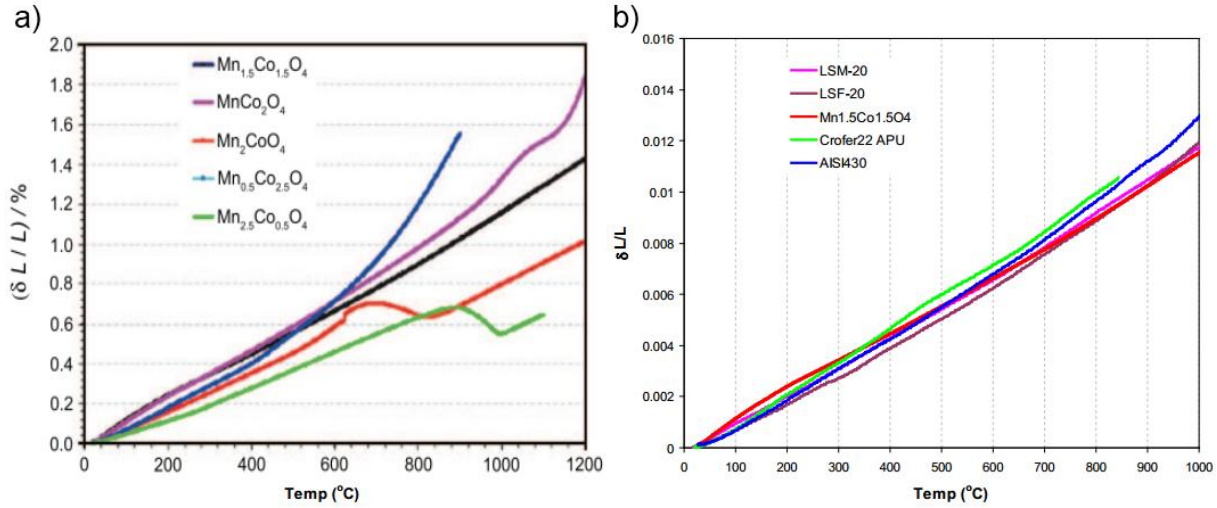

Figure 2.4: Thermal expansion measured for a) various manganese cobalt oxide compositions [22] and b) Mn1.5Co1.5O4 in comparison with some ferritic steels and cathode materials. LSM-20 and LSF-20 are ceramics used for cathode applications while Crofer22 APU and AISI430 are ferritic steels [17].

From Figure 2.4a, it is apparent that $Mn_{1.5}Co_{1.5}O_4$ exhibits the most linear and stable thermal expansion behavior. However, below 1000 °C, the behavior of $MnCo_2O_4$ is very close to that of $Mn_{1.5}Co_{1.5}O_4$. Since the working temperatures of the SOFC are limited to 800 °C and below, it implies that both compositions are suitable as coatings material.

The criterion of electrical conductivity is uncommon for conventional coating materials and is an area where manganese cobalt oxides excel. In Figure 2.5, the conductivity for certain manganese compounds are shown with respect to temperature. At 800 °C, values of 30-40 S/cm have been observed for $MnCo_2O_4$ [25, 26]. Another study claim that values as high as 60 S/cm were obtained at 800 °C [27]. In the same study, several spinel compositions were investigated with respect to CTE and electrical conductivity. The conclusion was that $Mn_{3-x}Co_xO_4$ ($1.5 < x < 2$) was best fitted for the purpose as interconnect coatings.

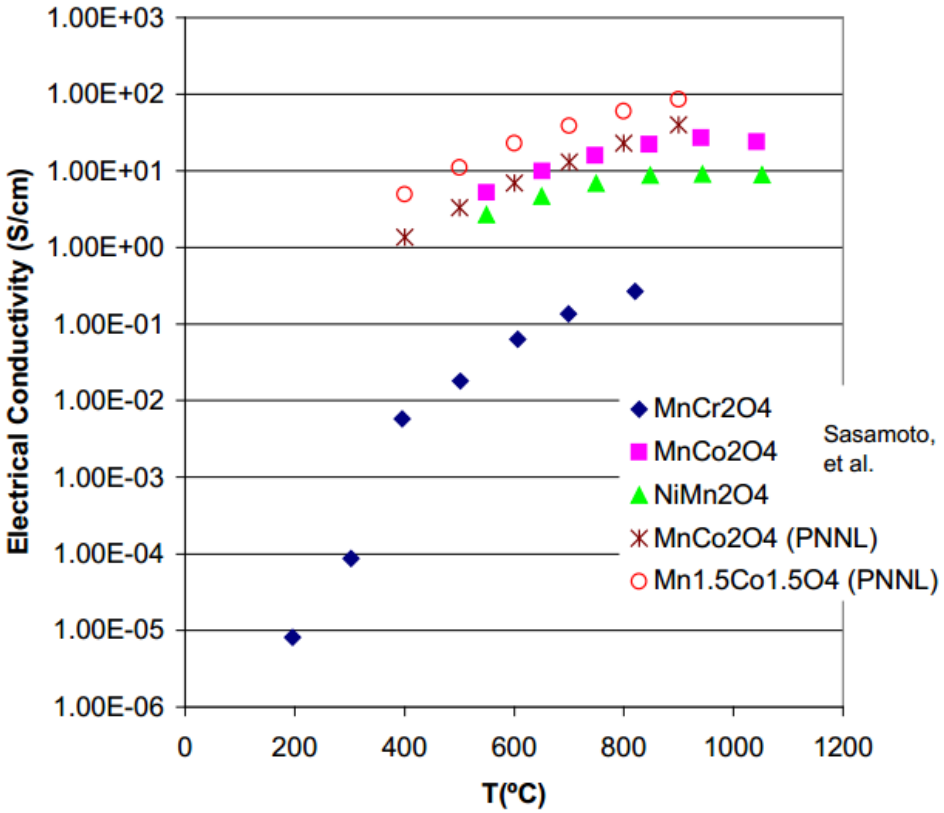

Figure 2.5: Electrical conductivity as a function of temperature for some relevant coating materials [28]

2.5 Spray pyrolysis

Spray pyrolysis is categorized as a wet chemical deposition method. It is considered simple and cost-effective as the procedure does not involve any costly steps such as vacuum. Additionally, no expensive equipment or high quality substrates are needed.

2.5.1 The principle

The operating principle of spray pyrolysis is based on the atomization of a precursor solution by means of a carrier gas. The produced aerosols are then transported to a heated substrate initiating film formation (Figure 2.6). Due to the heat, the constituents involved react and/or decompose to form the desired compound on the substrate surface. Normal operating temperatures span from 100-500 °C, which allow less robust materials to be used as substrates [7-9, 29].

The simplicity of the principle enables fabrication of doped coatings, as any element in any amount can be added in the precursor solution. Moreover, multilayered films with different compositions can also be produced by changing the precursor solution in between each spraying session [9]. In addition, process parameters can easily be adjusted, allowing fabrication of a variety of coatings with respect to microstructure, thickness and density etc.

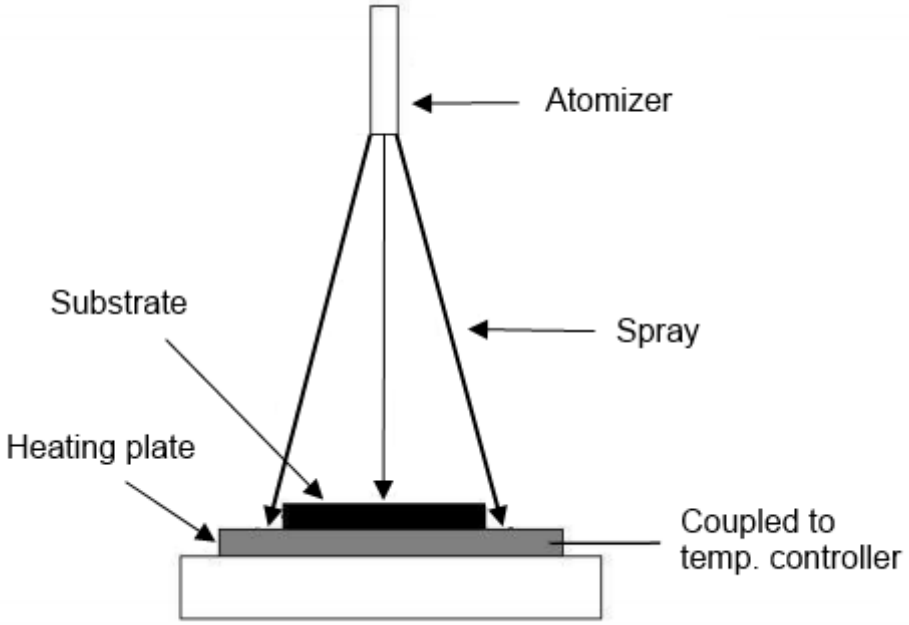

Figure 2.6: Principle of spray pyrolysis technique.

2.5.2 Process parameters

There are a number of parameters involved in spray pyrolysis. Each of them has an effect on the film formation and thus the final coating properties. According to the literature [8, 29-32], the most influential parameter is the deposition temperature. The temperature affects the aerosol transport, the evaporation of solvent and the droplet impact with following spreading. In addition, the decomposition of precursors is temperature dependent. It is worth to mention that the deposition temperature is not the same as the substrate temperature. However, these two values are nearly synonymous as the deposition temperature is only slightly lower, due to the presence of a liquid solution during spraying.

Next to the temperature, the second most significant parameter is the precursor solution since the type of solvent and its boiling temperatures, along with its constituents and concentration, affects the aerosol evolution physically as well as chemically [30]. Nonetheless, the behavior of the solution and the droplets in flight are correlated with the deposition temperature. The initial properties of the aerosol are however dictated by the nozzle, carrier gas and carrier gas pressure. Especially the nozzle type is critical for the atomization process as it determines the size of the droplets and their size distribution [9].

Less significant variables include the spray rate, quantity of precursor solution sprayed, the spraying distance, the ambient atmosphere and the cooling rate after deposition. In order to achieve superior coating properties, these parameters should also be optimized [8, 9].

2.5.3 Deposition mechanisms

Knowledge about the deposition mechanisms and film formation is vital in order to produce higher quality coatings. Unfortunately, these mechanisms are not fully understood because of the many process steps occurring simultaneously or sequentially. Efforts have been made to define the main steps which are: atomization of the precursor solution, transport of droplets and their evaporation, spreading of the droplets on the preheated substrate surface, and drying and decomposition of the precursor salt [30].

The evaporation of droplets, as well as the decomposition of the precursor are two processes that are highly temperature dependent. Too high temperatures cause a rapid evaporation of the droplets, which result in solid particles by the time of impact. Such a coating a coating will have poor properties, since the solid particles do not bond well to the substrate. On the other hand, too low temperatures allow wet droplets to hit the substrate. The deposited film thus contains solvent. Upon further drying and processing, the film will crack due to the solvent evaporation [33]. Needless to say, an intermediate temperature is thus best suited (Figure 2.7).

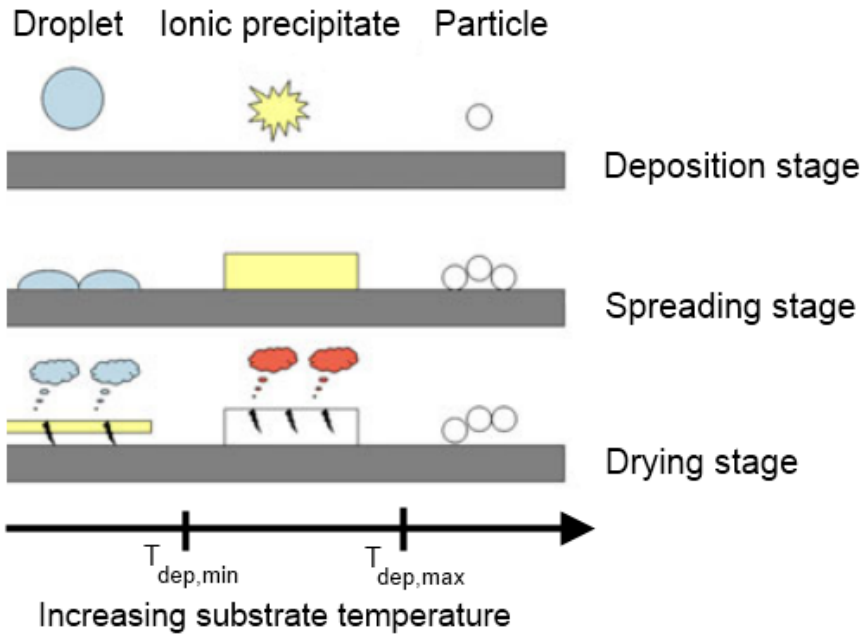

Figure 2.7: Various deposition processes for increasing substrate temperature [33].

In a study by Weber et al. thick lanthanum zirconate coatings were prepared by spray pyrolysis. In order to achieve optimal coatings, the influence of deposition temperature was investigated with respect to film formation, decomposition and the results on the coating microstructure and composition. The proposed mechanisms are shown in Figure 2.7. Weber reported that at an intermediate temperature, successful coatings were

obtained due to the formation of ionic salt precipitates. During the later stages of coating deposition, these precipitates would namely decompose partially without introducing any cracks [33].

Since ionic precipitates are required, it implies that a deposition temperature above the solvent boiling point is required. Otherwise, remaining solvent will evaporate and generate cracks. Still, too high temperatures must be avoided. Weber thus concluded that for any given precursor solution, it is necessary to uncover a suitable deposition temperature range in order to spray optimal coatings. This entail that there are no general temperature interval which can be used independently of different precursor solutions [8, 33].

2.5.4 A technique with good promise

The state of the art deposition methods for interconnect coatings are powder based and include methods such as slurry coating and electrophoretic deposition [6]. The necessity of a powder adds additional process steps and raises the manufacture costs. Magnetron sputtering is another technique that is currently employed for the deposition of coatings [6]. However, as for the powder based techniques, it is more expensive and more complicated than spray pyrolysis.

In light of the current deposition methods employed, spray pyrolysis is thus an interesting alternative to be investigated with respect to simple and cost-effective manufacture.

3 Experimental

3.1 Preparation of precursor solution

Aqueous solutions of 0.5 M $Mn(NO_3)_2 \cdot xH_2O$ and 0.5 M $Co(NO_3)_2 \cdot 6H_2O$ were used to prepare the precursor solution. Detailed information of the chemicals is listed in Table 3.1.

Table 3.1: Chemicals used to prepare the precursor solution.

Chemical	Formula	Purity [%]	Supplier	CAS
Manganese nitrate hydrate	$Mn(NO_3)_2 \cdot xH_2O$	98	Alfa-Aesar	15710-66-4
Cobalt nitrate hexahydrate	$Co(NO_3)_2 \cdot 6H_2O$	98	Sigma-Aldrich	10026-22-9

Thermogravimetric standardization was executed to reveal the accurate concentration of the aqueous solutions, since it was obscured by the content of crystal water. The temperature program applied for the standardization is shown in Figure 3.1. The cation concentration in each solution was uncovered by weighing the nitrates and the resulting oxides. Then the precursor solution was obtained by mixing the nitrate solutions in a Co:Mn molar ratio of 2:1.

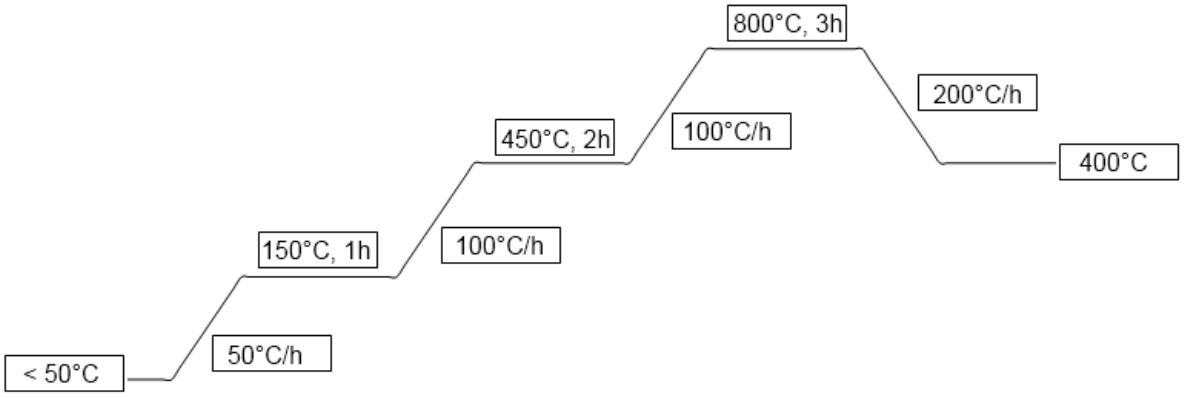

Figure 3.1: Temperature program applied for the standardization of the two nitrate solutions.

3.2 Substrate preparation

E-brite pieces with dimensions of 20 x 20 x 1.5 mm^3 were selected as the substrate material. This is a ferritic stainless steel alloyed with 26 wt% Cr and 1 wt% Mo which is among the FSSs utilized as interconnect material [34].

The substrates were grinded and/or polished in order to obtain various degrees of surface roughness. Table 3.2 displays the grinding procedure implemented for the steel pieces. An automated grinding apparatus consisting of Struers TegraForce – 5 (sample holder) and Struers TegraPol – 31 (rotator) was used to ensure reproducible surface

finishes. Be aware that the grinding time is approximate, depending on whether or not the desired surface profile had been obtained. For polished substrates (roughness code P) this implies a mirror finish.

Table 3.2: Grinding and polishing procedures for the substrates.

Roughness Code	Force [N]	Grinding disc	Lubricant	Time [min]	Speed [rpm]
P	180 70 120	#220 SiC paper MD-Largo MD-Dac	Water DiaPro All/Lar DiaPro Dac	5 10 20	300 150 150
#800	180	#800 SiC paper	Water	5	300
#500	180	#500 SiC paper	Water	5	300
NA	Rough substrates as received. No processing.				

All pieces were subject to an ultrasonic bath in acetone for thirty minutes before spraying. This ensured a clean surface, free of grease and organic matter that otherwise would have impeded the adhesion.

3.3 Spray pyrolysis

3.3.1 Spray pyrolysis apparatus

Spraying of the coatings was executed on a spray pyrolysis apparatus designed and built by Weber et al. at NTNU. An illustration of the setup is shown in Figure 3.2.

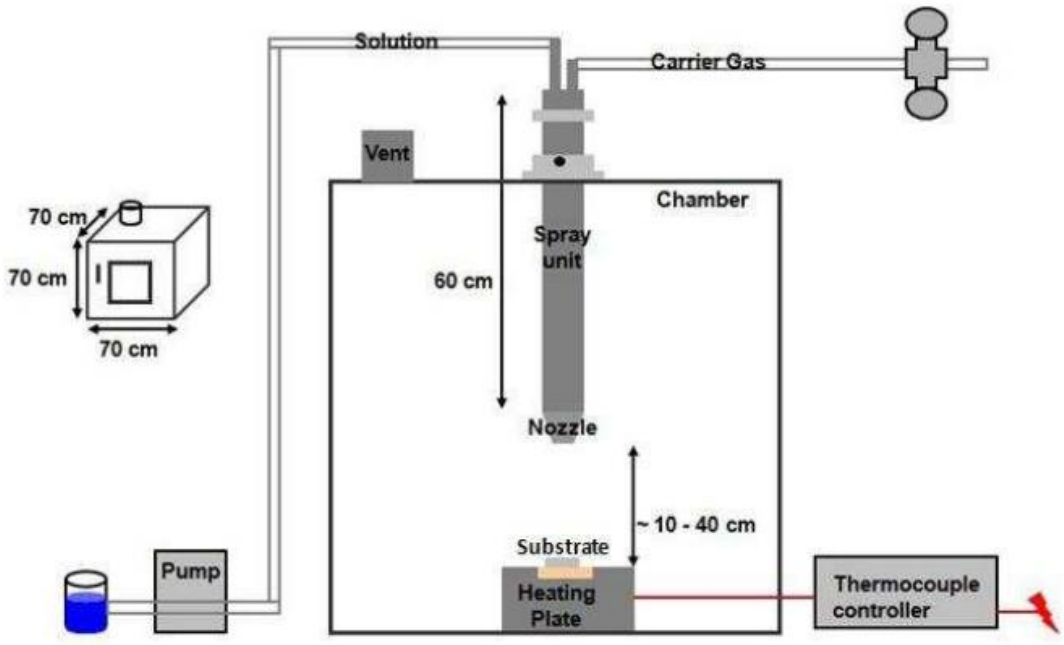

Figure 3.2: Schematic of the spray pyrolysis setup used in this work [33].

The spraying unit located inside the chamber can be moved vertically to adjust the spraying distance. Directly underneath, there is a heating plate protected by an AlN cover and a steel sheet. The substrate is placed on top of the covering plates. The heating plate is controlled by a thermocouple unit located outside the chamber. During operation, a peristaltic pump (Heidolph Pumpdrive 5201) feed the precursor solution through a flexible pipe and into the spraying unit. The solution mixes with the carrier gas and is ejected as aerosols through the nozzle. In this work, synthetic air was used as carrier gas. Additional details about this setup can be found in the doctoral thesis of Weber [8].

Note that the substrate temperature in this setup is different from the target temperature selected for the heating plate. Since the substrate is separated from the heating plate by the two covers of AlN and steel, the substrate temperature is noticeably lower than the target temperature. Moreover, the temperature on the substrate is also highly dependent on the presence of the gas flow. For a target temperature of 800 °C, the substrate temperature is 165 °C when exposed to the gas flow and 425 °C when the gas supply is off.

3.3.2 Spraying procedure and parameters

Based on earlier work by the author, several spray parameters were assigned default values for the deposition on different substrate surfaces. This was true for the spraying distance, carrier gas pressure, substrate temperature and the spraying rate with values of 25 cm, 0.6 bar, 165 °C and 0.3 mL/min respectively [10].

Prior to each spraying session, the nozzle was cleaned and the pipe flushed with distilled water. When the heating plate reached its target temperature, the substrate was manually placed underneath the spraying unit. After spraying of each sample, the green coating was left to dry for one minute with the gas supply still on. The drying was thus performed at 165 °C.

The sample name A-B-C consists of the roughness code for the substrate (A), spray volume (B) and sort of post-processing/heat treatment (C). For samples with two layers, a "+B-C"- extension is added to the name. Be aware that consecutive heat treatments on the same layer, will give a sample name such as A-B-C1.C2.C3 etc. The various heat treatments conducted are explained in Table 3.3.

Table 3.3: Heat treatments conducted on the deposited coatings.

Code	**Post-processing/heat treatment**
D	Decomposition of as-deposited green coatings without gas supply, i.e. 425 °C Time: 5 min
A2	Heat treatment at 800 °C in air. Heating and cooling rates of 200 °C/h Time: 2 h
A5	Heat treatment at 800 °C in air. Heating and cooling rates of 200 °C/h Time: 5 h
AR5	Heat treatment at 1100 °C in argon. Heating and cooling rates of 150 °C/h Time: 5 h

3.3.3 Single layers coatings on substrates of various roughnesses

An overview of the coatings deposited on substrates with different surface roughnesses is shown in Table 3.4. All coatings were made by spraying 5mL of the precursor solution. Green coatings were produced as well as simple post-processed samples.

Table 3.4: Coatings prepared on substrates with various surface roughnesses.

No	Sample name	Roughness code	Volume sprayed [mL]	Post-processing/ heat treatment
1	P-5	P	5	
2	P-5-D	P	5	D
3	#800-5	#800	5	
4	#800-5-D	#800	5	D
5	#500-5	#500	5	
6	#500-5-D	#500	5	D
7	NA-5	NA	5	
8	NA-5-D	NA	5	D

3.3.4 Multilayered coatings

The monolayer coatings prepared prior to deposition of the second layers can be seen in Table 3.5. Fabricated multilayered coatings are presented in Table 3.6. Samples 17-20 were subject to the simple post-processing between application of the first and second layers. More extensive heat treatments were performed both before and after deposition of the second layer for coatings 21-30. Between application of the first and second layers, all specimens were stored minimum a day at room temperature in a dry cabinet.

Table 3.5: Monolayered coatings exposed to a selection of heat treatments before application of a second layer.

No	Sample name	Volume sprayed [mL]	Post-processing/ heat treatment
9	P-5-D.A2	5	D.A2
10	P-2-D.A2	2	D.A2
11	P-5-D.A5	5	D.A5
12	P-2-D.A5	2	D.A5
13	P-5-D.AR5	5	D.AR5
14	P-2-D.AR5	2	D.AR5
15	P-5-D.AR5.A5	5	D.AR5.A5
16	P-2-D.AR5.A5	2	D.AR5.A5

Table 3.6: Multilayered coatings and their corresponding fabrication data.

		Layer 1		Layer 2	
No	**Sample name**	**Volume sprayed [mL]**	**Post-processing/ heat treatment**	**Volume sprayed [mL]**	**Post-processing/ heat treatment**
17	P-5-D+5	5	D	5	
18	P-5-D+5-D	5	D	5	D
19	P-2-D+5	2	D	5	
20	P-2-D+5-D	2	D	5	D
21	P-5-D.A2+5-D	5	D.A2	5	D
22	P-5-D.A2+5-D.A2	5	D.A2	5	D.A2
23	P-2-D.A2+5-D	2	D.A2	5	D
24	P-2-D.A2+5-D.A2	2	D.A2	5	D.A2
25	P-5-D.A5+5-D.A5	5	D.A5	5	D.A5
26	P-2-D.A5+5-D.A5	2	D.A5	5	D.A5
27	P-5-D.AR5+5-D.AR5.A5	5	D.AR5	5	D.AR5
28	P-2-D.AR5+5-D.AR5.A5	2	D.AR5	5	D.AR5
29	P-5-D.AR5.A5+5-D.A5	5	D.AR5.A5	5	D.A5
30	P-2-D.AR5.A5+5-D.A5	2	D.AR5.A5	5	D.A5

3.4 Coating characterization

3.4.1 Fourier transform infrared spectroscopy (FTIR)

FTIR analysis of a green coating was performed in order to uncover its constituents. The analysis was performed on KBr-pellets for wavelengths 500-4000 cm^{-1}. The amount of coating material mixed in the KBr-pellet was 0.5 wt% and was achieved by scratching off flakes of coatings from the substrate. Prior to examination, a background scan was run with a pure KBr-pellet. The apparatus in use was an IFS 66V from Bruker.

3.4.2 Thermogravimetric analysis (TGA)

The thermal behavior of a green coating as well as its components was elucidated by TGA. The coating material was scratched off the substrate and analyzed for temperatures 20-1000 °C with a heating rate of 2 °C/min in synthetic air. The experiment was conducted on a STA 449C Jupiter from NETZSH.

3.4.3 X-ray diffraction (XRD)

The phase composition of heat treated coatings was established by XRD measurements using a D8 Focus Diffractometer with a Lynxeye™ detector using Cu K_{α}-radiation accelerated at 40 kV and 40 mA. Scans were run for 2θ-values from 15° to 60° with a 0.02° step count.

3.4.4 Scanning electron microscopy (SEM)

The surface and cross section of the coatings, as well as the substrate surfaces, were examined in SEM. In order to obtain cross section images, the coatings were embedded in epoxy, mechanically cut with a diamond saw, polished according to Table 3.2, and coated with carbon. The thickness was measured along with the cross section imaging.

The microscope employed was Zeiss Supra 55VP – a low-vacuum field emission scanning electron microscope (LVFESEM). Utilized settings for the imaging were a working distance of 9-10 mm; a standard aperture size of 30 µm, a low-current mode and an accelerating voltage of 10 kV. Micrographs were taken in the middle of each sample.

3.4.5 Energy dispersive X-ray Spectroscopy (EDS)

EDS-analysis was performed parallel to the SEM imaging and included both cross sections and surfaces of the coatings. The microscope used, was a low-vacuum scanning electron microscope (LVSEM), brand Hitachi SU-6600. Recommended settings for the characterization is a working distance of 10 mm, a high-current mode (70-80 %) and an accelerating voltage of 15 kV. Micrographs were taken in the middle of each sample.

4 Results

4.1 Effect of substrate roughness

Micrographs of the assorted substrate surfaces are presented in Figure 4.1. Larger magnification micrographs can be viewed in appendix A. The images confirm that different degrees of roughness were achieved prior to coating deposition.

Figure 4.2 display the coatings prepared to elucidate the effect of the substrate roughness. It was observed that green coatings on P- and #800-substrates were unstable and showed signs of flaking shortly after spraying. In a matter of days, the coatings – and especially P-5 – had delaminated severely. The phenomenon was less noticeable for #500-5 (weeks) and non-existent for NA-5.

The post-processing proved to stabilize the coatings; however the cracks became more prominent. An exception is P-5-D which showed more or less unchanged crack features. However a number of circular spots appeared on the coating surface. NA-5 and NA-5-D contained few cracks in general, but are greatly affected by the substrate surface.

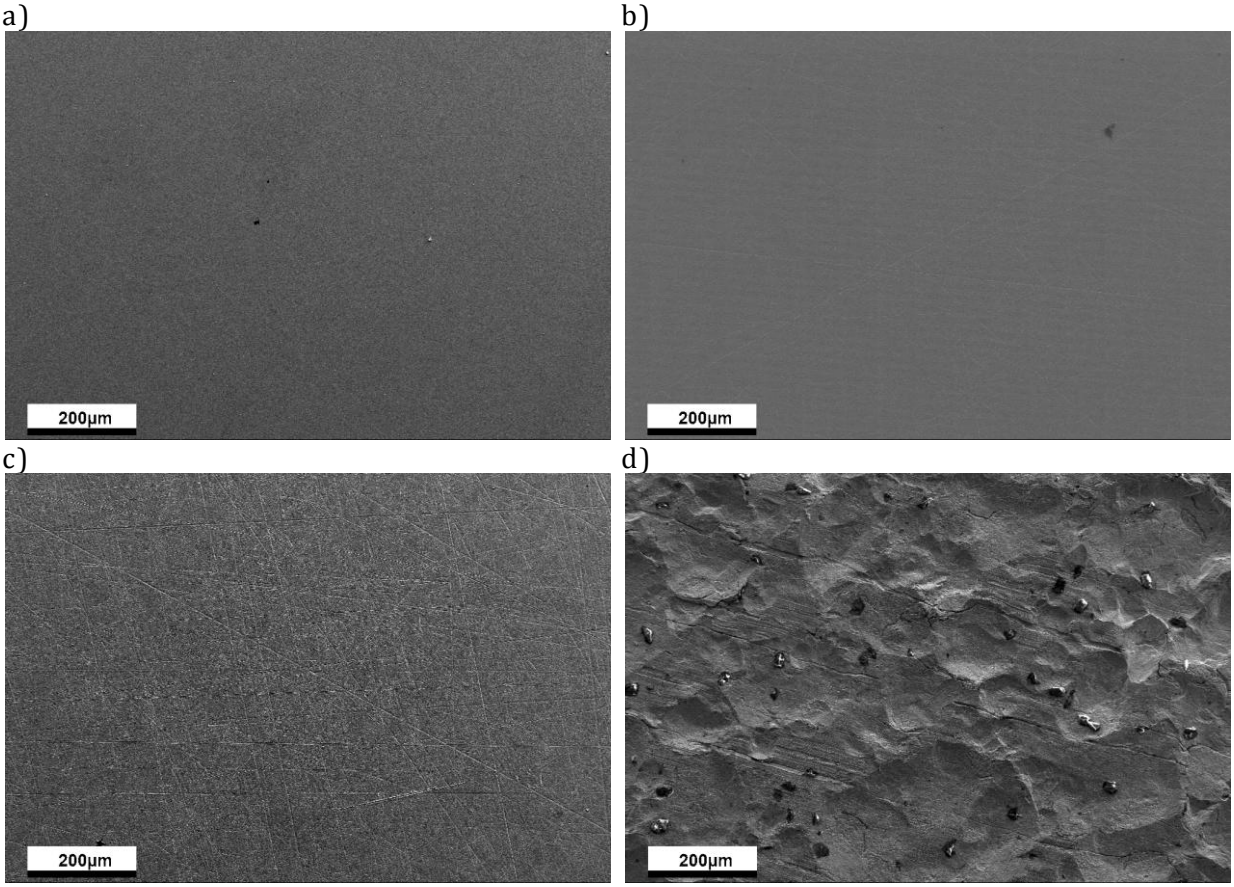

Figure 4.1: SEM micrographs of the surface microstructure for a) P-substrate, b) #800-substrate, c) #500-substrate and d) NA-substrate. All substrates were cleaned in an acetone bath prior to image capture.

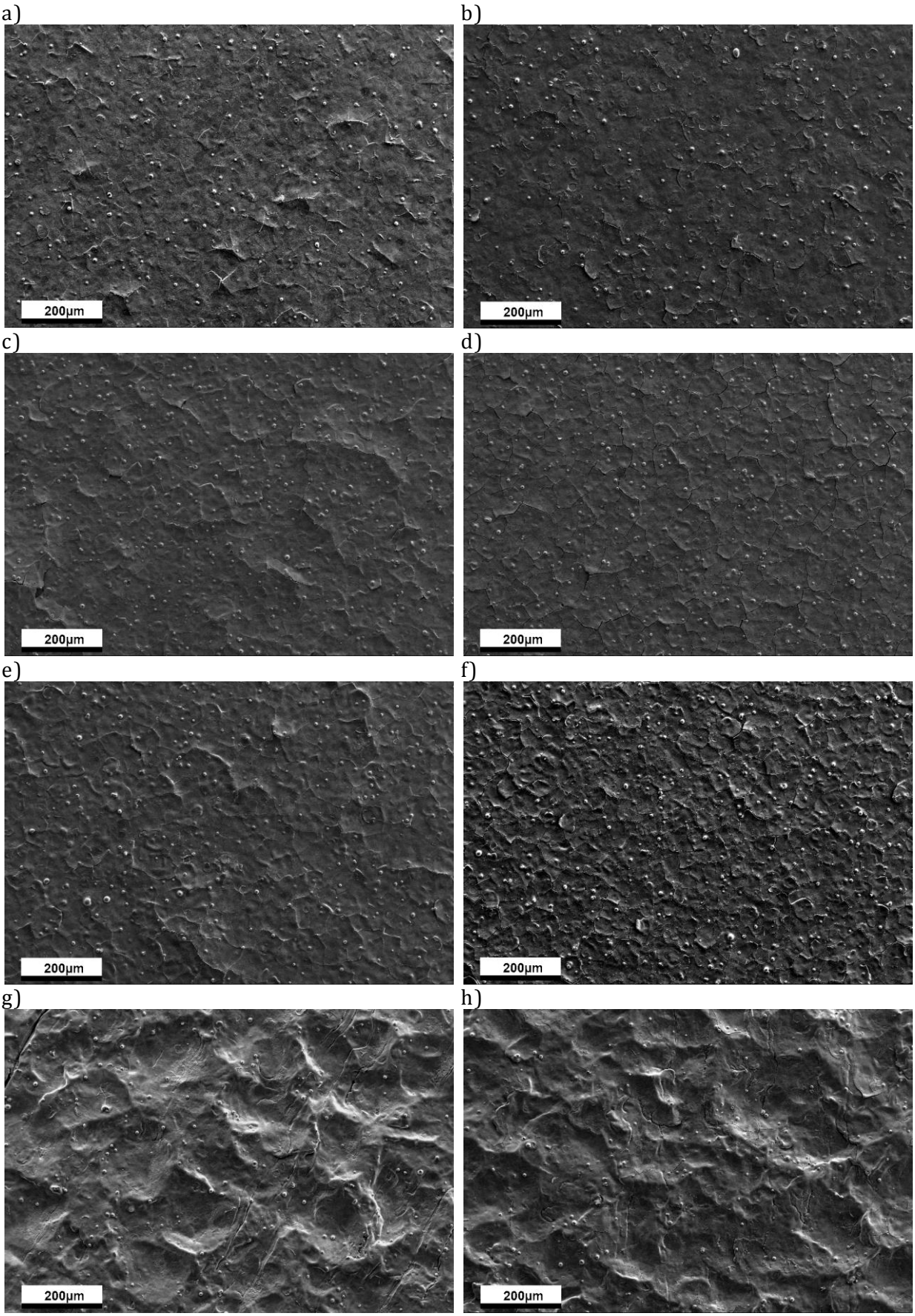

Figure 4.2: SEM micrographs of the surface microstructure for a) P-5, b) P-5-D, c) #800-5, d) #800-5-D, e) #500-5, f) #500-5-D, g) NA-5and h) NA-5-D.

The cross section images of P-5-D and NA-5-D in Figure 4.3 demonstrate clear differences between the coatings. Despite less cracks, the thickness of NA-5-D varies substantially. In contrast, P-5-D has a relative uniform thickness, but contains cracks that run through the whole layer. The degree of adhesion seems to be inferior for P-5-D as sections of the layer are partly or fully detached from the substrate.

Regardless of the thickness homogeneity, the cross section images reveal that the overall thickness is well below the desired values.

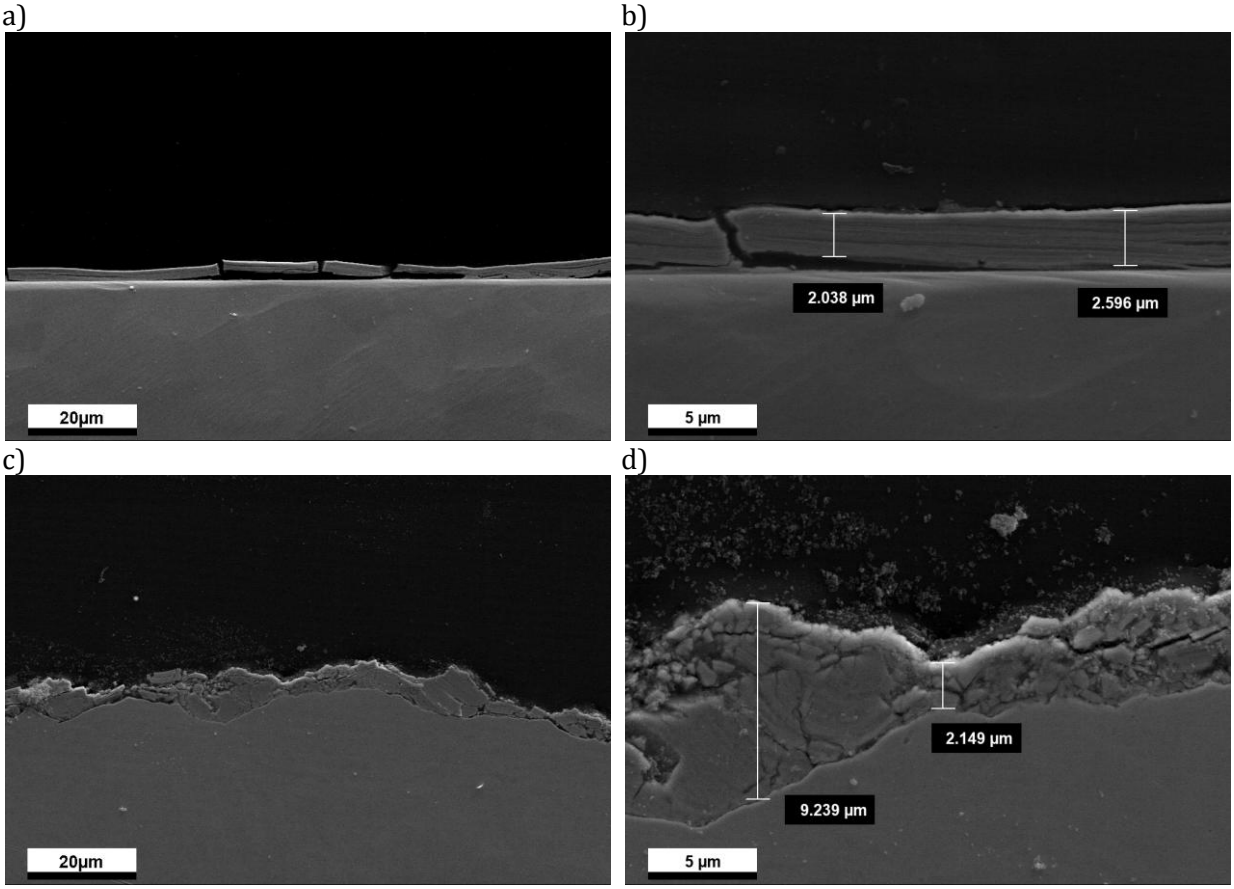

Figure 4.3: SEM micrographs of cross section microstructure for a) P-5-D and b) NA-5-D with corresponding thickness values.

An FTIR spectrum of the green coating P-5 is given in Figure 4.4 and reveals four characteristic bands. The broad band located around 3100-3600 cm^{-1} is assigned to the stretching vibrations of O-H [35]. The band at 1608 cm^{-1} corresponds to the bending mode of H_2O [36], whereas the sharp band centered at 1384 cm^{-1} and the band around 1042 cm^{-1} is attributed to the ν_3 and ν_1 vibrational modes of NO_3^- respectively [35]. It is thought that the sharpness of the band at 1384 cm^{-1} is caused by surface adsorbed NO_2 or CO_2 [37].

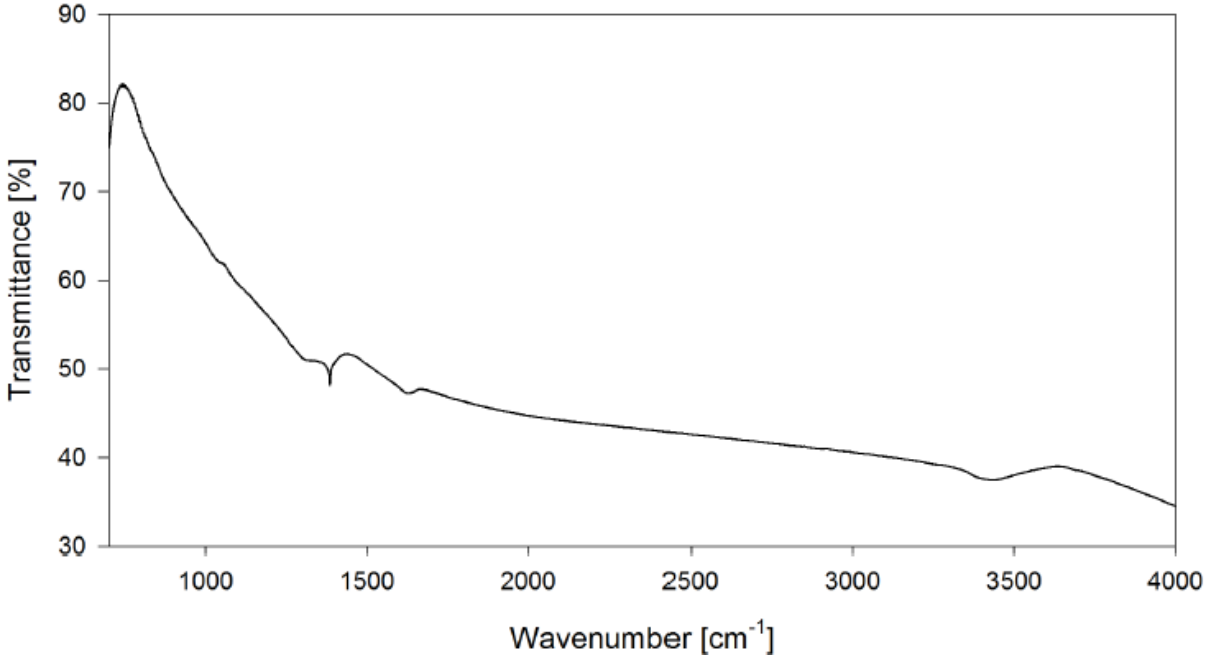

Figure 4.4: FTIR spectrum of green coating P-5.

The thermogravimetric analysis of P-5 yielded three distinct regions for mass loss (Figure 4.5). The first mass loss, situated around 100 °C, is caused by evaporation of remnant water from spray pyrolysis and/or absorbed water after spraying. The second mass loss from 150-350 °C can be attributed to the decomposition of nitrates. Lastly, the mass loss detected from 350 °C towards 650 °C, is believed to be caused by the decomposition of carbonates [33].

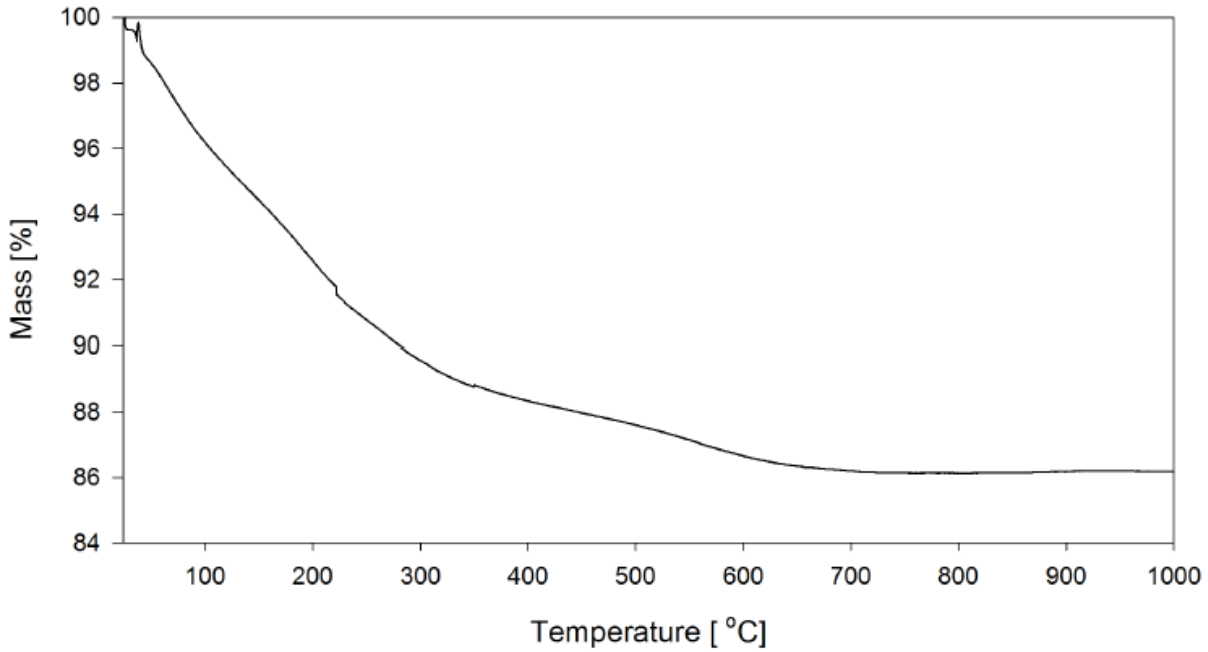

Figure 4.5: TGA of green coating P-5.

4.2 Multilayered coatings

4.2.1 Initial preparation of multilayered coatings

Figure 4.6a-b present pictures of P-5-D+5 and P-5-D+5-D. As seen, the coatings are of poor quality. P-5-D+5 delaminated in one whole piece few minutes after deposition, whereas P-5-D+5-D began cracking severely.

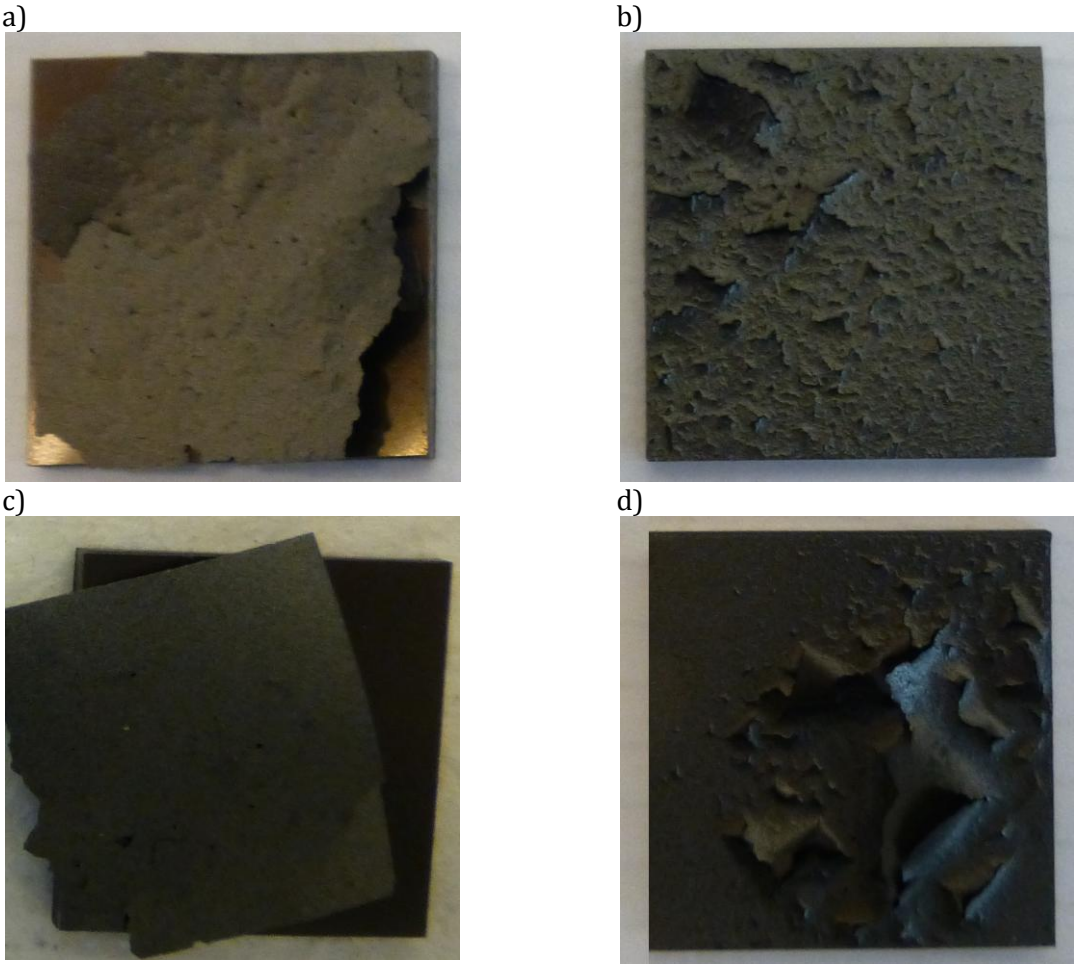

Figure 4.6: Poor quality multilayered coatings a) P-5-D+5, b) P-5-D+5-D, c) P-2-D+5 and d) P-2-D+5-D.

Samples P-2-D+5 and P-2-D+5-D suffered from delamination and cracking as well, albeit somewhat slower (Figure 4.6c-d). Also it was observed that sample P-2-D+5-D contain areas that are not substantially cracked by comparison to P-5-D+5-D.

4.2.2 Coatings prepared by heat treatment in air

Heat treatment of the first layer before deposition of a second layer proved efficient in order to obtain stable multilayer coatings. Samples P-5-D.A2+5-D, P-5-D.A2+5-D.A2, P-2-D.A2+5-D and P-2-D.A2+5-D.A2, heat treated at 800 °C for 2 h, exhibited adequate adhesion, and their microstructure is revealed in Figure 4.7. The corresponding heat treated monolayers are presented in Figure 4.8 and serve as a reference for the resulting surface features on the second layers.

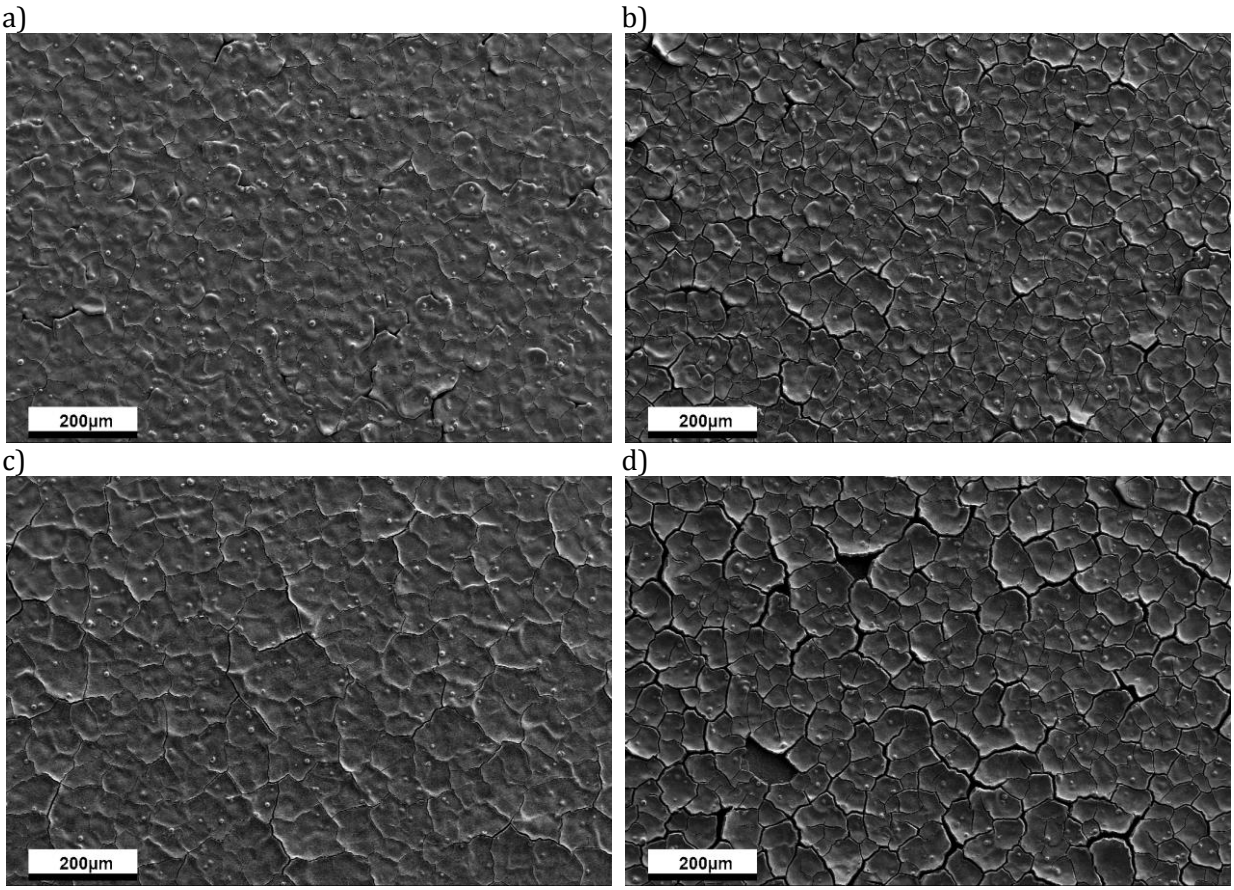

Figure 4.7: SEM micrographs of the surface microstructure for a) P-5-D.A2+5-D, b) P-5-D.A2+5-D.A2, c) P-2-D.A2+5-D and d) P-2-D.A2+5-D.A2.

Coatings based on a primary layer of 2 mL show a worse microstructure than the ones based on a layer of 5 mL. Sample P-2-D.A2+5-D.A2 have exposed areas and coarser cracks than P-5-D.A2+5-D.A2 (Figure 4.7d and Figure 4.7b respectively). This is also reflected in the coatings where the final layer was exposed to the mere prost-processing (Figure 4.7a-c). In contrast, the single layer of 2 mL (Figure 4.8b) has better crack characteristics after heat treatment than the monolayer of 5 mL (Figure 4.8a).

Considering P-5-D.A2+5-D.A2 (Figure 4.7b), it appears that the cracks have softer edges and it seems that the second round of spraying covers cracks from the initial layer. The same depiction cannot be attributed to P-2-D.A2+5-D.A2 (Figure 4.7d). Furthermore, it is worth mentioning that the crack features of P-2-D.A2+5-D.A2 are similar to that of the monolayer P-5-D.A2 (Figure 4.8a).

a) b)

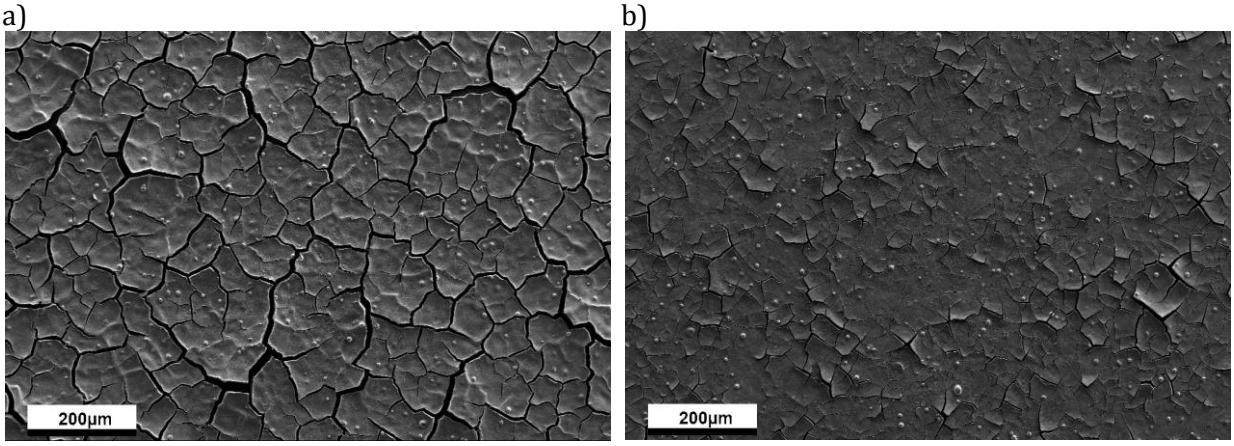

Figure 4.8: SEM micrographs of the surface microstructure for a) P-5-D.A2 and b) P-2-D.A2.

Cross section images of P-5-D.A2+5-D, P-5-D.A2+5-D.A2, P-2-D.A2+5-D and P-2-D.A2+5-D.A2 are provided in Figure 4.9. For samples P-5-D.A2+5-D and P-2-D.A2+5-D the two layers are separated whereas the heat treated coatings show one thick layer. Regardless, all four coatings contain run-through cracks and seem to be comprised of lamellae. In addition, the adhesion to the substrate is questionable when considering the cross sections on a micrometer scale.

a) b)

c) d)

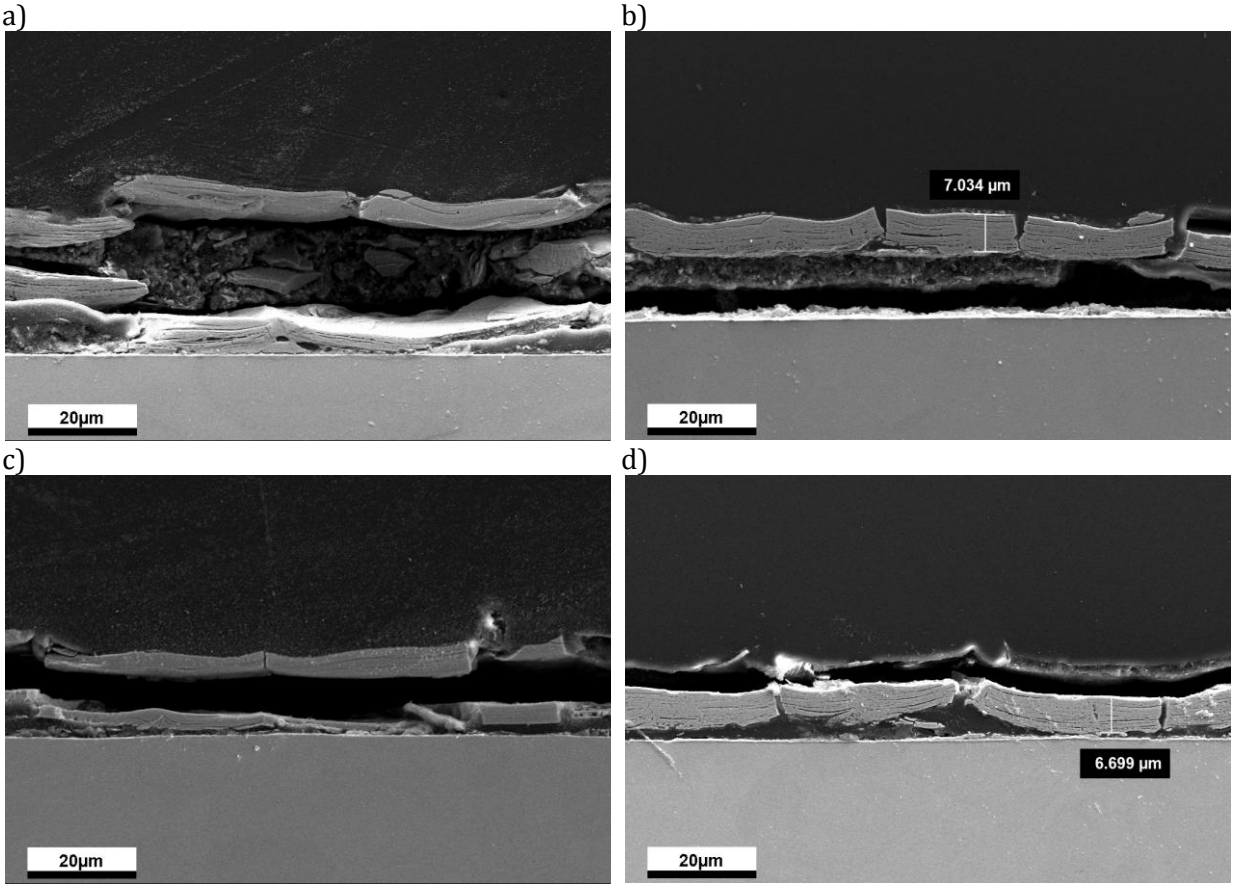

Figure 4.9: SEM micrographs of cross section microstructure for a) P-5-D.A2+5-D, b) P-5-D.A2+5-D.A2, c) P-2-D.A2+5-D and d) P-2-D.A2+5-D.A2.

The differences between 2 + 5 mL and 5 + 5 mL layered coatings are exemplified further when samples with identical layer build-up are heat treated for 5 h at 800 °C. Figure 4.10a-b show that the 5 + 5 mL layered coatings, represented by P-5-D.A5+5-D.A5, indeed has softer edges and less prominent cracks than 2 + 5 mL coatings, here represented by P-2-D.A5+5-D.A5 (Figure 4.10c-d). However, several areas underneath the upper layer are exposed, but they seem to be of the primary layer.

The cross section images in Figure 4.11 show that the two layers in both coatings have good adhesion to each other and can be said to have sintered into one layer. However, it is possible to distinguish between the two layers for sample P-5-D.A5+5-D.A5 (Figure 4.11a) due to the partial vertical cracks indicating that the cracks in the primary layer has been covered by the second layer deposition. In addition, the lamellar structure is still present, but the coatings appear denser than the ones that were heat treated for 2 h (cracks not accounted for).

A thickness of 8.374 µm and 6.811 µm was measured for P-5-D.A5+5-D.A5 and P-2-D.A5+5-D.A5 respectively as seen in Figure 4.11. The coatings are thus reaching the desired thickness target of minimum 10 µm.

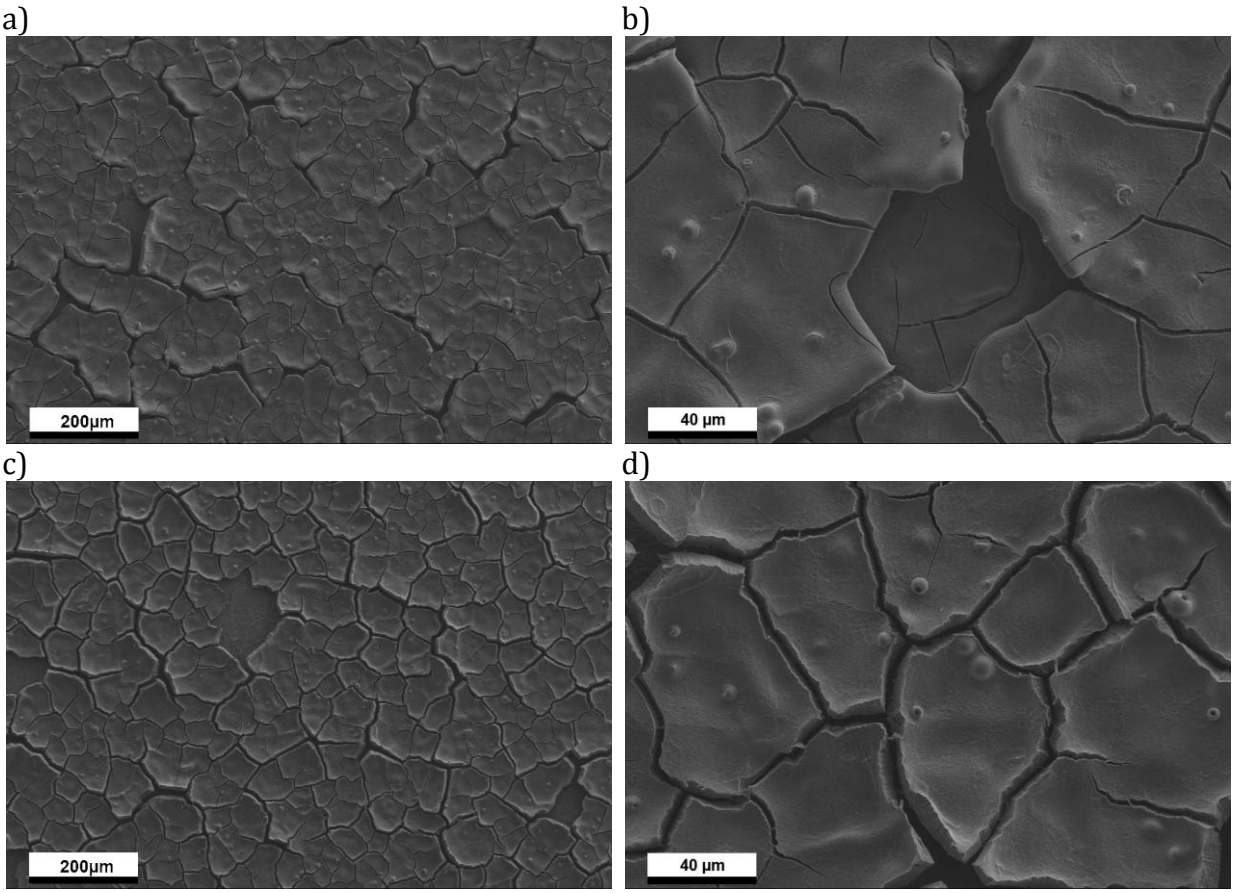

Figure 4.10: SEM micrographs of the surface microstructure for a-b) P-5-D.A5+5-D.A5 and c-d) P-2-D.A5+5-D.A5.

a) b)

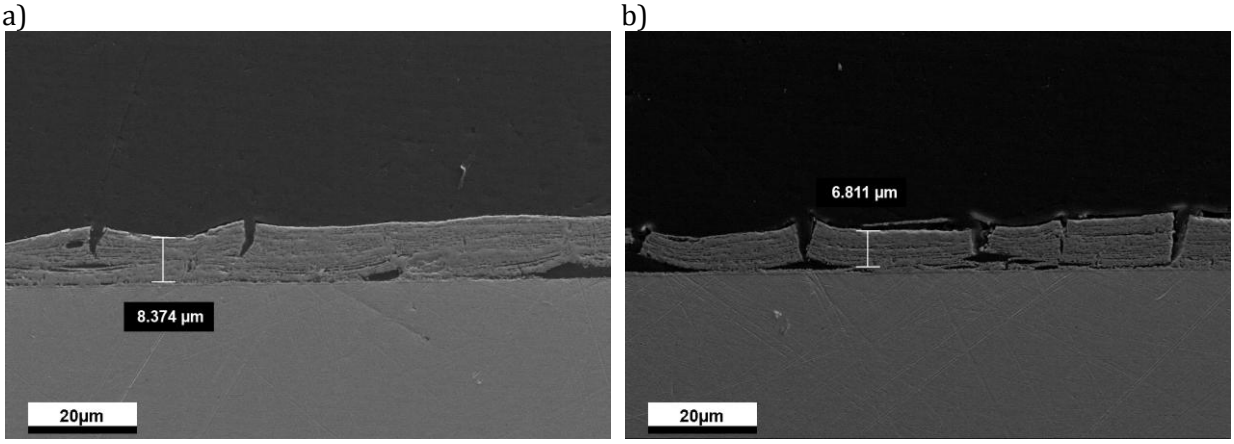

Figure 4.11: SEM micrographs of the cross section microstructure for a) P-5-D.A5+5-D.A5 and b) P-2-D.A5+5-D.A5.

An EDS map of the coating surface for sample P-5-D.A5+5-D.A5 (Figure 4.12) reveals that chrome is exposed through many of the cracks, implying that vertical cracks run through both layers. This means that not all cracks from the primary layer are covered as shown in Figure 4.11a. However, it is observed that many of the areas where the primary layer is exposed do indeed provide successful coverage of the substrate as no chrome is detected.

a) b)

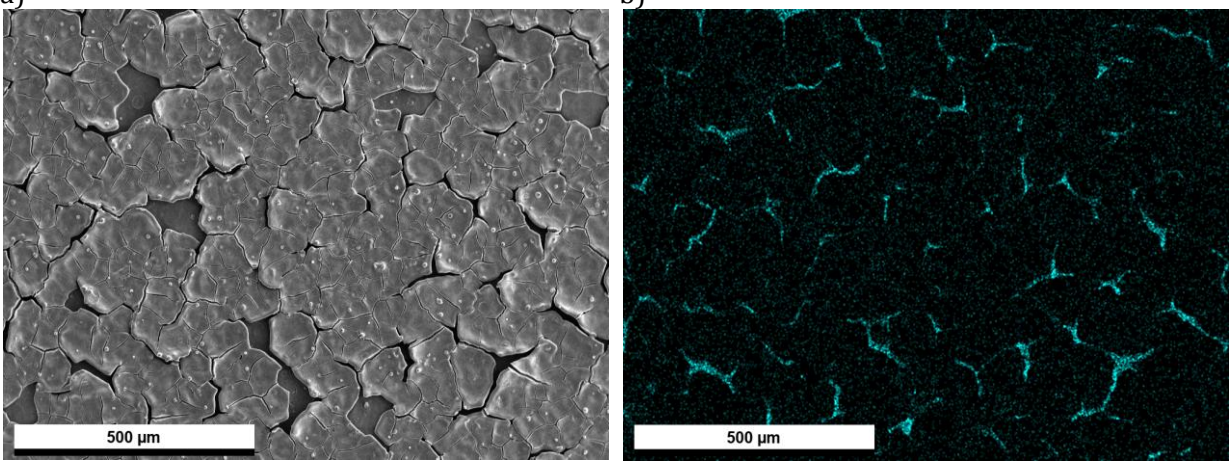

Figure 4.12: EDS map of P-5-D.A5+5-D.A5 surface. a) SEM image b) Cr-mapping

The corresponding monolayers are presented in Figure 4.13. P-5-D.A5 and P-2-D.A5 both possess less prominent crack features than P-5-D.A2 and P-2-D.A2, but the general trend indicates that monolayers sprayed with 5 mL indeed exhibit more numerous and coarser cracks. However, these cracks are not observed in the cross section for the corresponding multilayer (Figure 4.11a), suggesting that the cracks were healed by the second layer as mentioned earlier.

a) b)

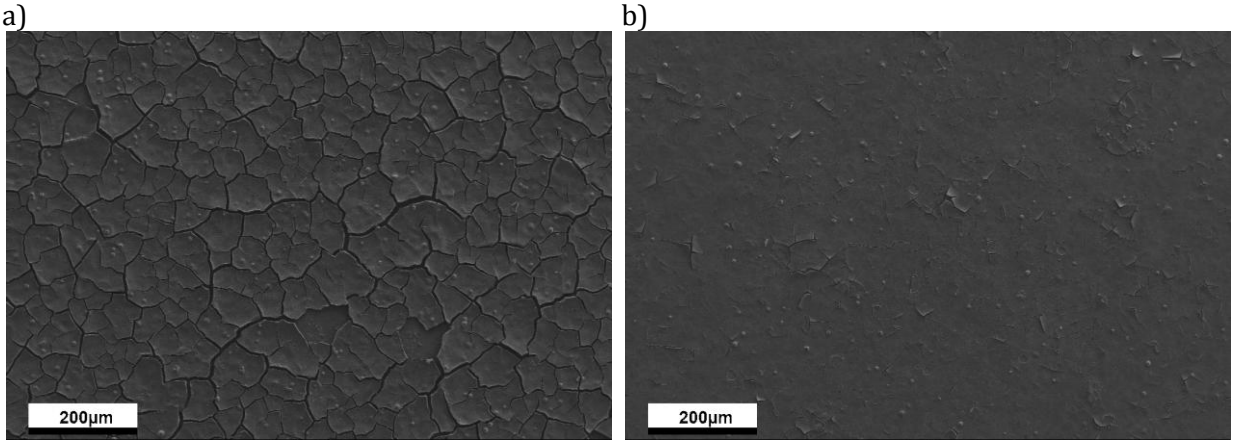

Figure 4.13: SEM micrographs of the surface microstructure for single layer coatings heat treated at 800 °C for 5 h. a) P-5-D.A5 and b) P-2-D.A5.

4.2.3 Coatings prepared by heat treatment in argon

Multilayered coatings with first layer heat treated only in argon

The heat treatment in argon at 1100 °C for 5 h yielded the monolayered coatings shown in Figure 4.14. The coatings P-5-D.AR5 and P-2-D.AR5 appear significantly different from those heat treated in air as they are virtually crack-free and seem denser.

a) b)

c) d)

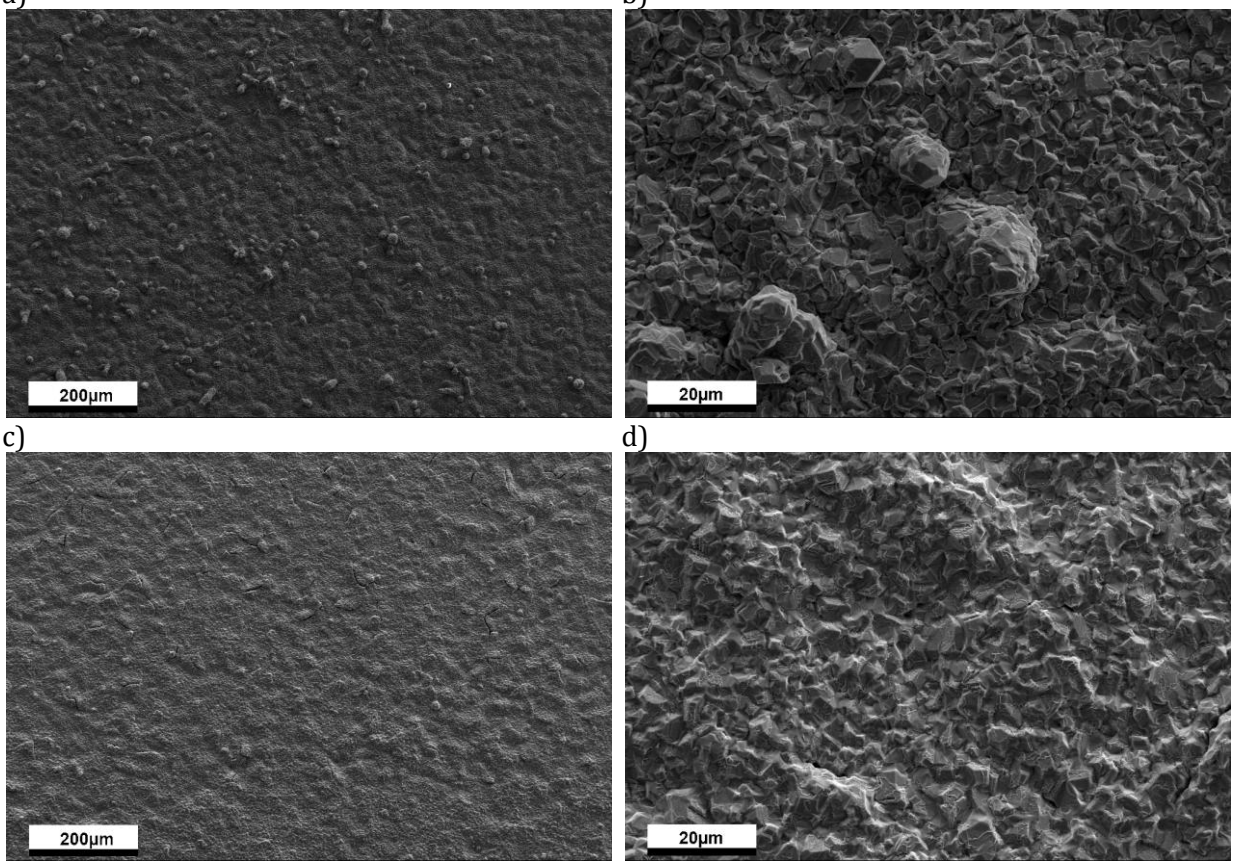

Figure 4.14: SEM micrographs of the surface microstructure for single layer coatings heat treated in argon at 1100 °C for 5 h. a-b) P-5-D.AR5 and c-d) P-2-D.AR5.

Figure 4.15 shows multilayered coatings building on the monolayers in Figure 4.14. These were heat treated in argon and then air for 5 h at 1100 °C and 800 °C respectively after deposition of the final layer. The microstructure appears nearly identical to its monolayered predecessor.

Regarding the cross sections (Figure 4.16), they are noticeably different from the coatings that were only heat treated in air. The lamella structure is absent and no cracks are present. Additionally, the layers seem to adhere well to the substrate and each other. An exception is P-5-D.AR5+5-D.AR5.A5 (Figure 4.16a) where the top layer is partly separated from the primary layer. This also means that the measured thickness of around 17.93 µm is somewhat lower. The thickness of P-2-D.AR5+5-D.AR5.A5 was found to be 7.927 µm, but as the two layers appear as one, the thickness value is much more accurate.

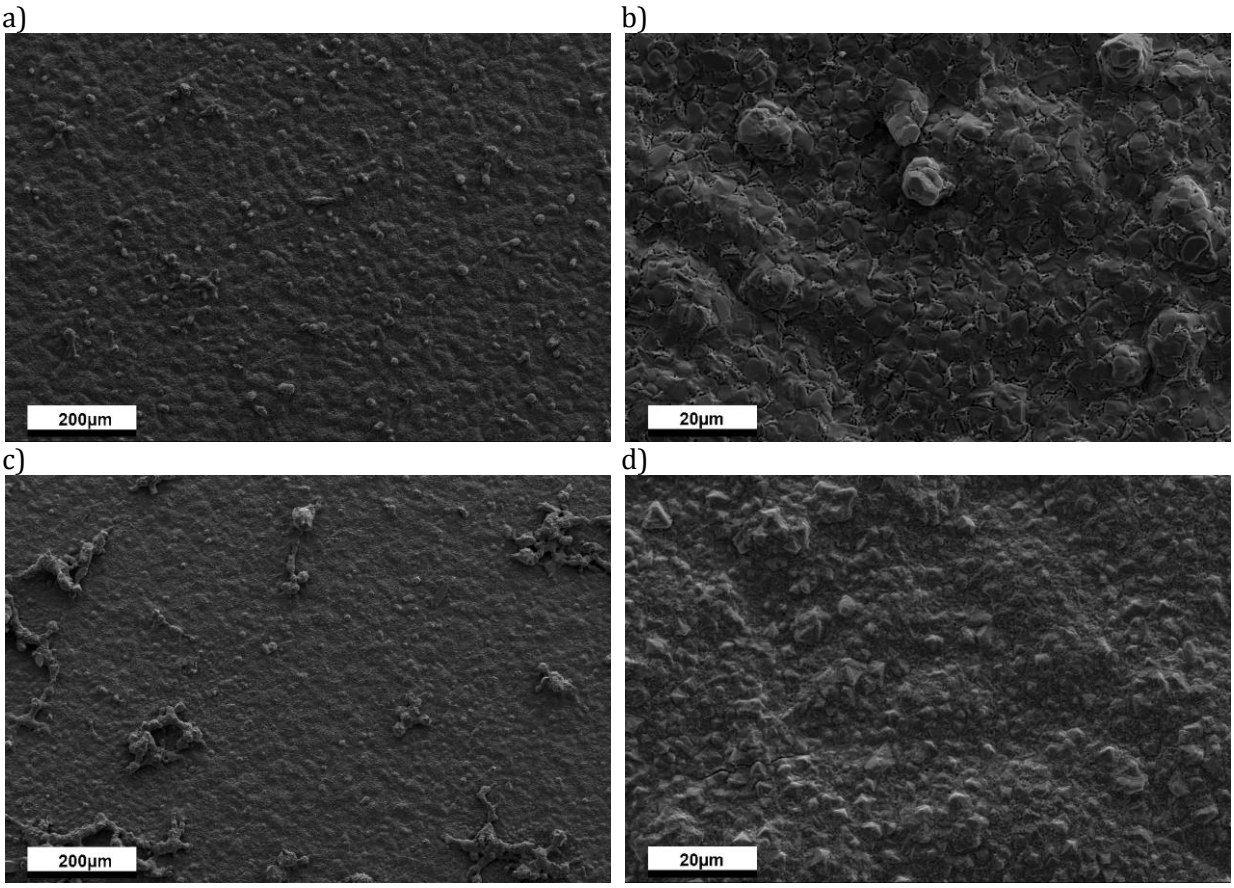

Figure 4.15: SEM micrographs of the surface microstructure for a-b) P-5-D.AR5+5-D.AR5.A5 and c-d) P-2-D.AR5+5-D.AR5.A5.

a) b)

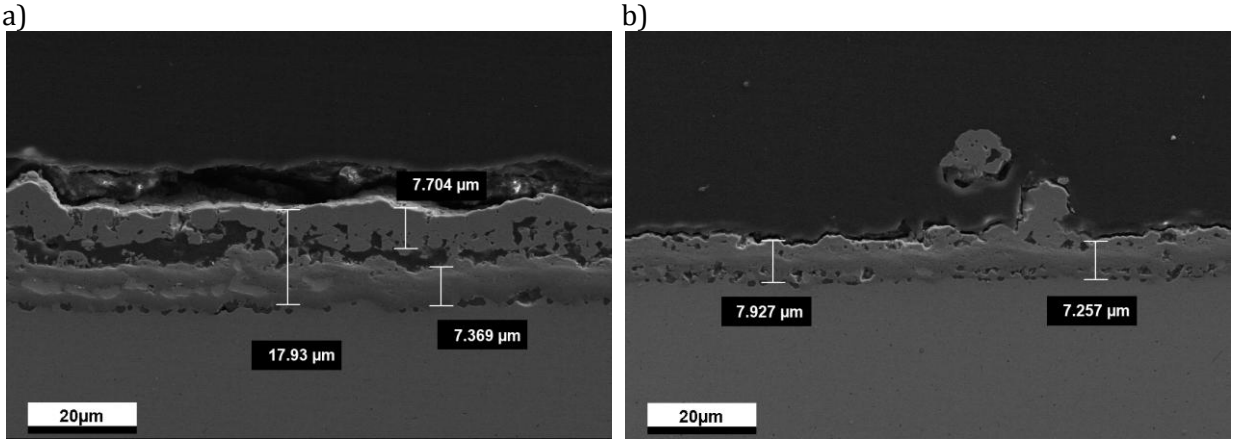

Figure 4.16: SEM micrographs of the cross section microstructure for a) P-5-D.AR5+5-D.AR5.A5 and b) P-2-D.AR5+5-D.AR5.A5.

Despite the good microstructure, XRD-analysis proved that a phase pure coating of $MnCo_2O_4$ was not maintained. This is particularly true for the monolayered coatings where the manganese cobalt oxide appear as $Mn_{1.45}Co_{1.55}O_4$. In addition CoO and Co_3O_4 were detected (Figure 4.17a). On the other hand, $Mn_{1.45}Co_{1.55}O4$ reverts to $MnCo_2O_4$ for the multilayered coatings after the final heat treatment in air (Figure 4.17b). However, Co_3O_4 is still present. This is clearly reflected on the close-up image and the corresponding EDS-map of sample P-5-D.AR5+5-D.AR5.A5 in Figure 4.18. The bright clots on the surface correspond to the yellow areas in the EDS map and have a content of cobalt and oxygen corresponding to Co_3O_4.

a)

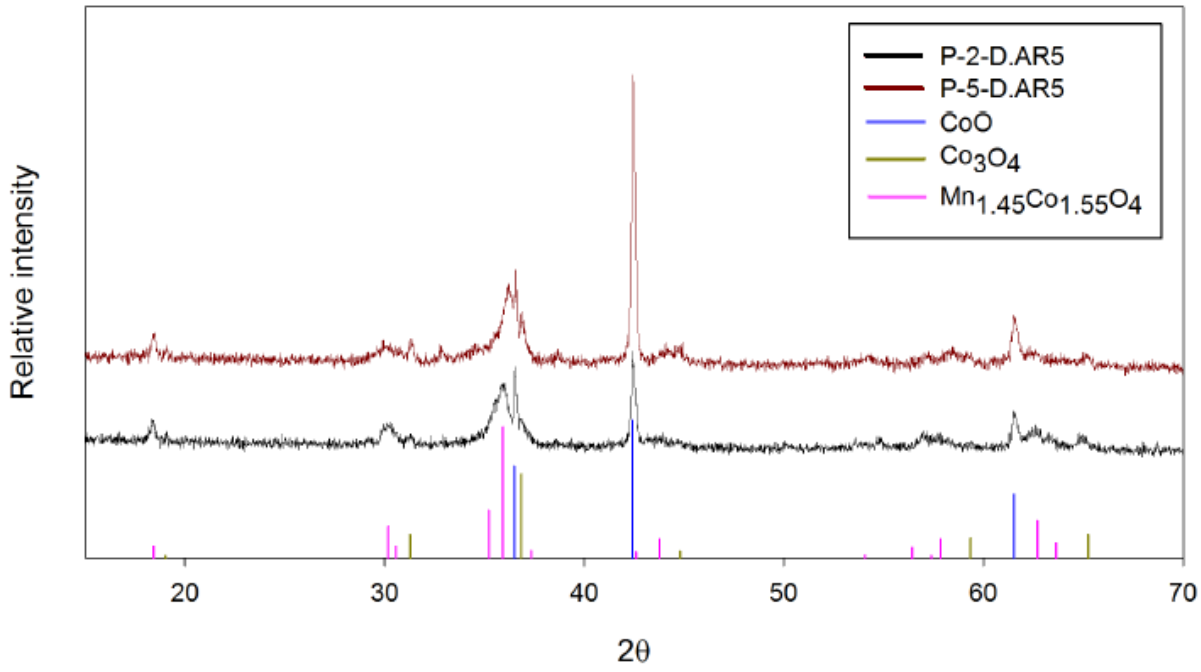

b)

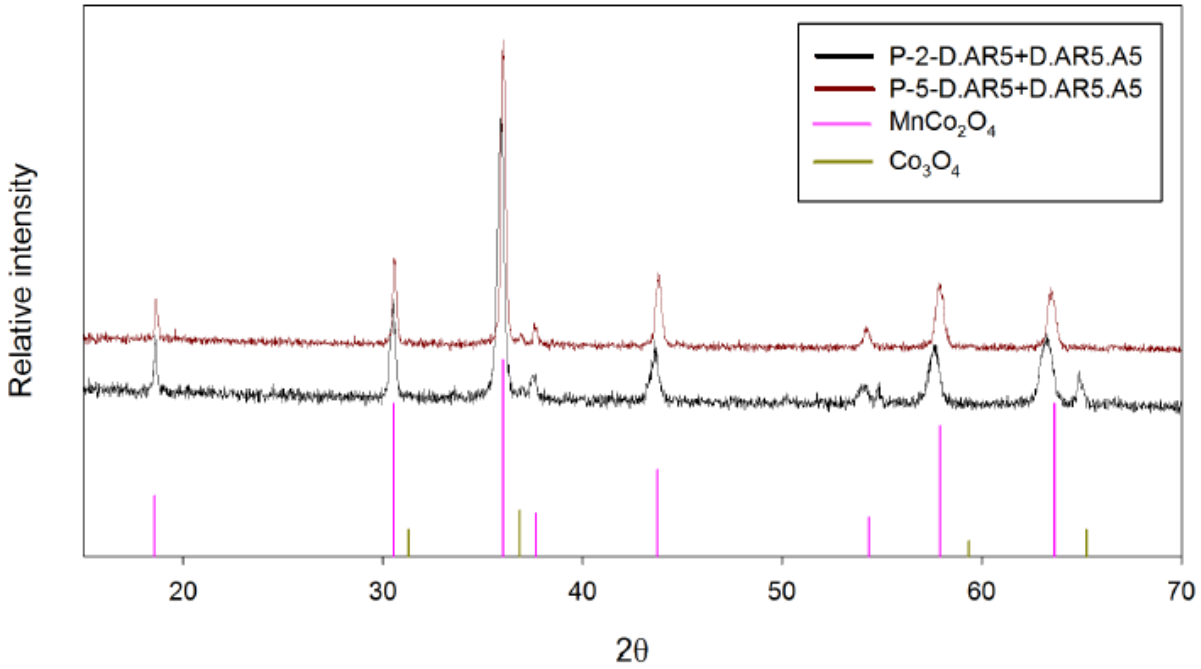

Figure 4.17: Diffractogram of a) monolayer coatings P-5-D.AR5 and P-2-D.AR5 and b) multilayer coatings P-5-D.AR5+5-D.AR5.A5 and P-2-D.AR5+5-D.AR5.A5.

a) b)

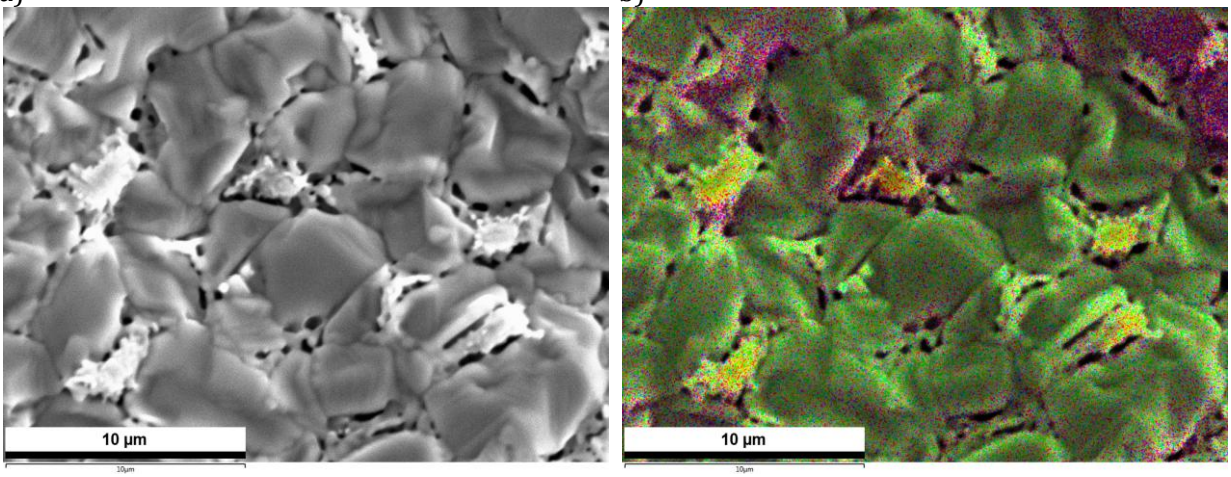

Figure 4.18: Close-up image of P-5-D.AR5+5-D.AR5.A5 in a) SEM and b) EDS.

The cross section of sample P-5-D.AR5+5-D.AR5.A5 also reveal bright inclusions in the layers which indicate presence of secondary phases. EDS-mapping of the cross section is provided in Figure 4.19 and do indeed reveal additional phase inhomogeneities. Point analysis yielded inclusions of a Co-Cr phase, a layer of chromium oxide and a top layer of $MnCo_2O_4$ (Table 4.1).

Table 4.1: EDS analysis of points marked in Figure 4.19a.

Point	**Mn [at%]**	**Co [at%]**	**O [at%]**	**Cr [at%]**	**Fe [at%]**	**Total [at%]**
1		75.60		21.54	1.78	100
2			57.30	42.41	0.29	100
3	18.40	29.24	51.02		0.74	100

Figure 4.20 presents the EDS-map of the cross section of P-2-D.AR5+5-D.AR5.A5. No inclusions were detected, but as for P-5-D.AR5+5-D.AR5.A5, a chromia scale was observed.

a) b)

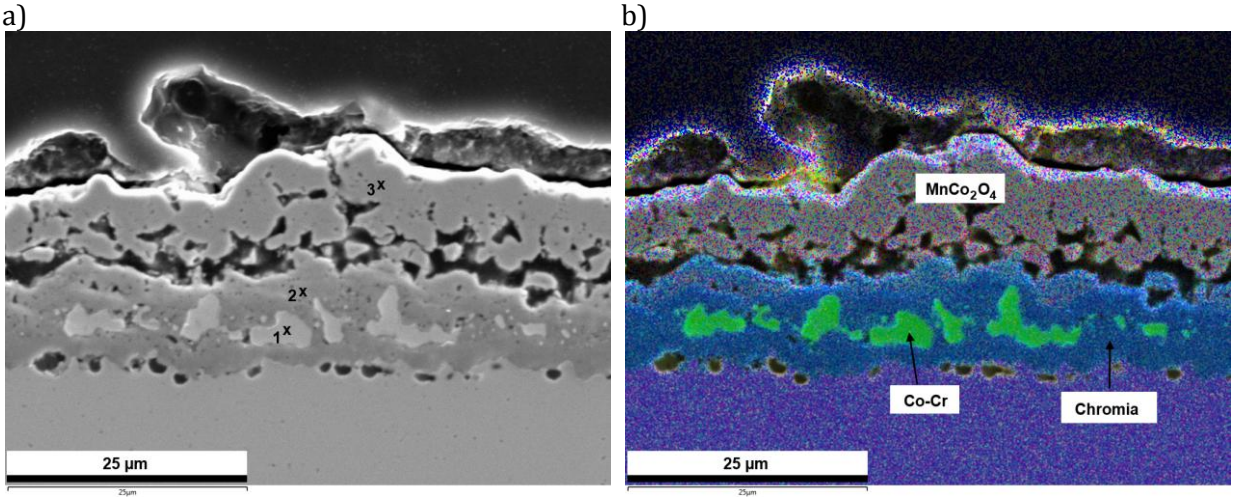

Figure 4.19: a) SEM micrograph and b) EDS-map of P-5-D.AR5+5-D.AR5.A5 cross section. Analyzed points are marked on the SEM image.

a) b)

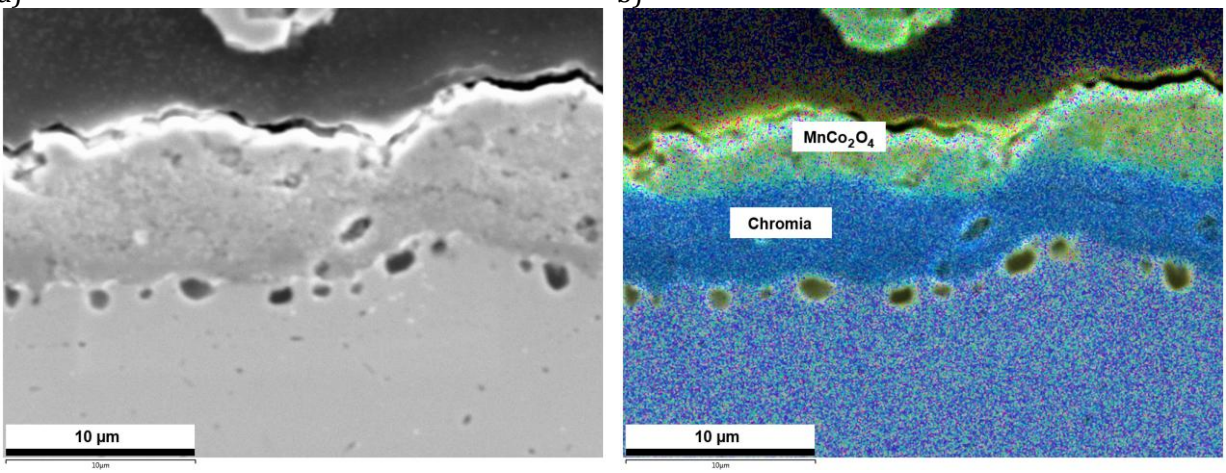

Figure 4.20: a) SEM micrograph and b) EDS-map of P-2-D.AR5+5-D.AR5.A5 cross section.

Multilayered coatings with first layer heat treated in argon and in air

Single layered samples of P-5-D.AR5.A5 and P-2-D.AR5.A5, heat treated for 5 h in argon at 1100 °C and then 5 h in air at 800°C, are shown in Figure 4.21. As a result of the additional heat treatment in air, crack evolution has caused smooth, thin continuous cracks to appear in sample P-5-D.AR5.A5. On the other hand, P-2-D.AR5.A5 contains wide, separated cracks.

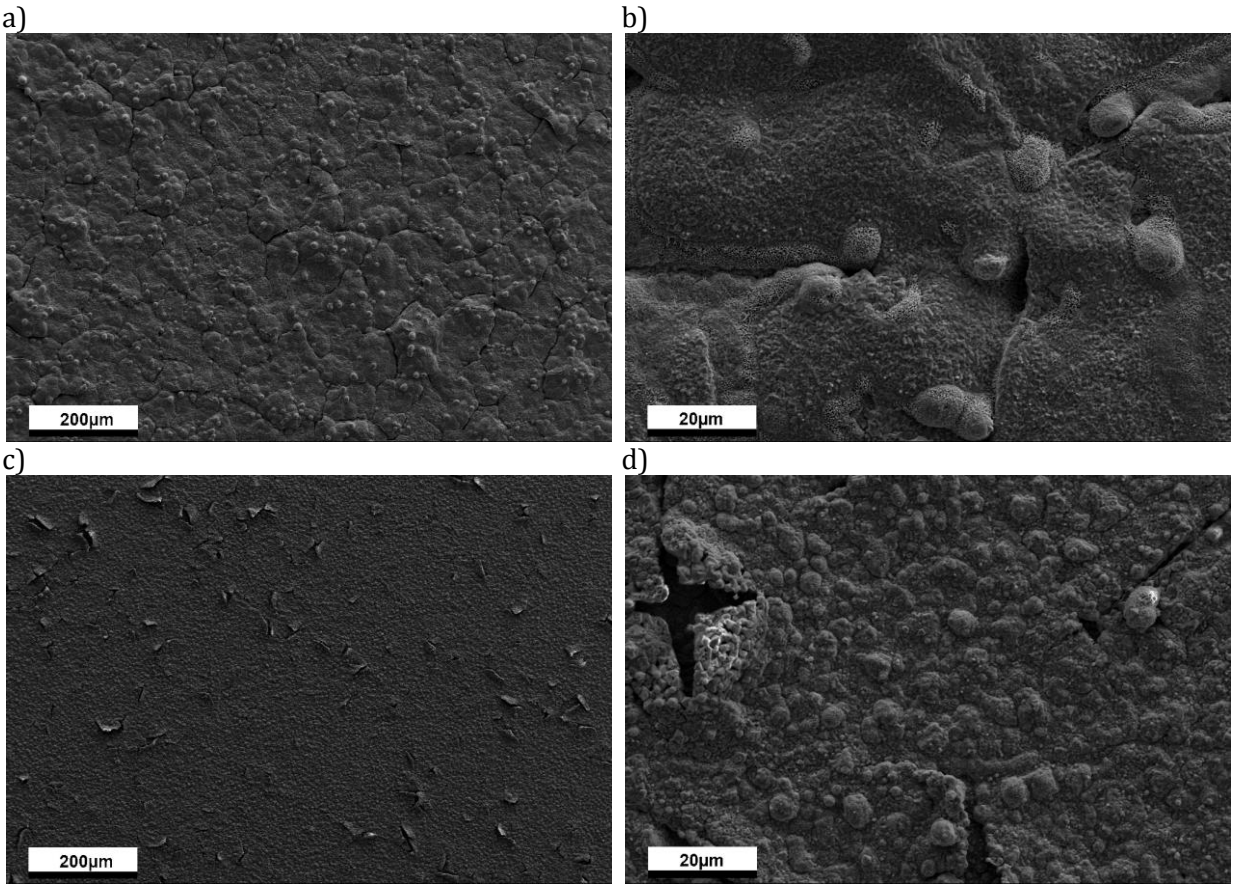

Figure 4.21: SEM micrographs of the surface microstructure for single layer coatings heat treated for 5 h in argon at 1100 °C and then 5 h in air at 800°C. a-b) P-5-D.AR5.A5 and c-d) P-2-D.AR5.A5.

Figure 4.22 present the diffractograms of coating P-5-D.AR5.A5 and P-2-D.AR5.A5. As seen, several secondary phases were detected for both samples. P-5-D.AR5.A5 possesses the $MnCo_2O_4$ phase, but also contains Co_3O_4 and Mn_2O_3. In the case for the thinner coating of P-2-D.AR5.A5, $MnCr_2O_4$ were detected in addition to Cr_2O_3, Mn_2O_3, metallic Co and Fe. The presence of iron suggests that the coating thickness may be too low, allowing iron to be detected during XRD analysis.

a)

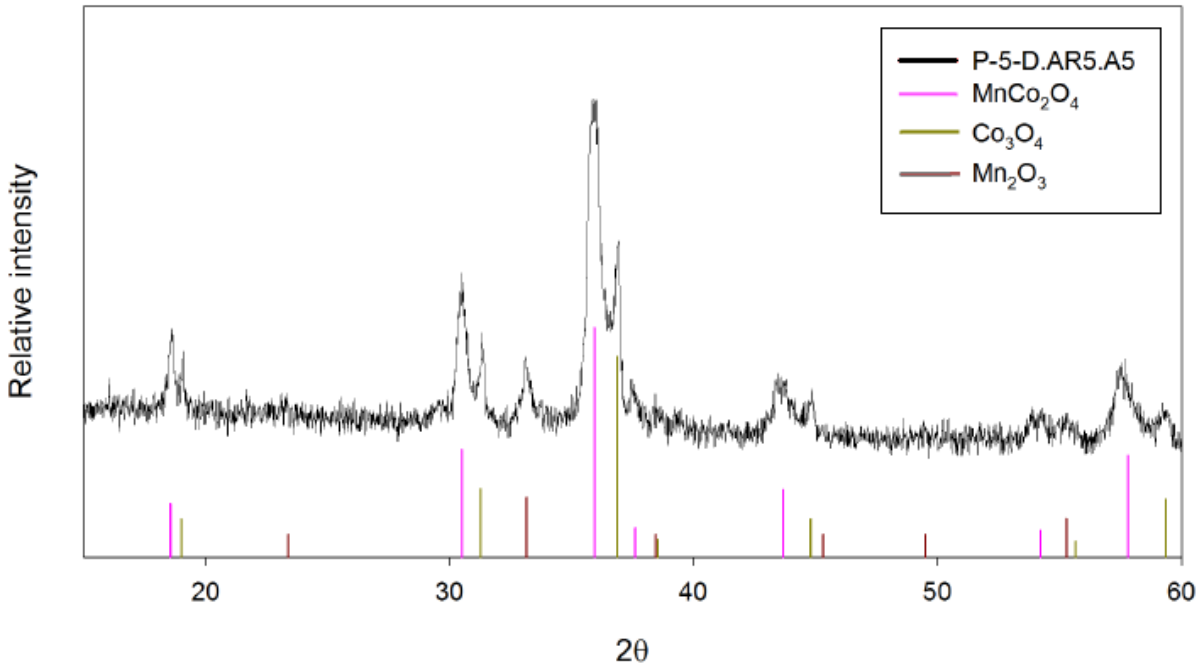

b)

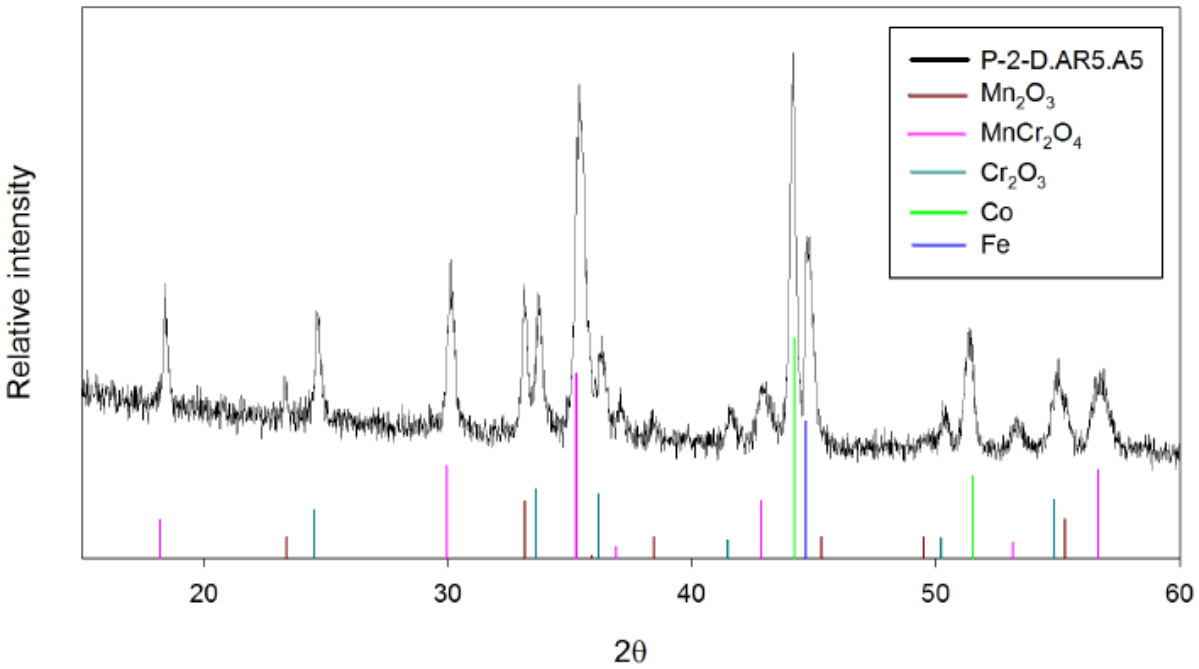

Figure 4.22: Diffractograms of a) P-5-D.AR5.A5 and b) P-2-D.AR5.A5

Multilayered coatings with second layer heat treated only in air

The multilayered coatings based on sample P-5-D.AR5.A5 and P-2-D.AR5.A5 are presented in Figure 4.23. As the sample names indicate, P-5-D.AR5.A5+5-D.A5 and P-2-D.AR5.A5+5-D.A5 were only subject to a heat treatment in air and not in argon after deposition of the final layer. Consequently, the coating surfaces look nothing like P-5-D.AR5+5-D.AR5.A5 (Figure 4.15a), but display great similarities with coatings such as P-5-D.A5+5-D.A5 (Figure 4.10a).

As seen in Figure 4.23, both coatings have a microstructure owed to their initial layers. Nevertheless, it appears that the primary layers were successfully covered by application of the top layer. This is well illustrated in Figure 4.23c-d. In addition, the cracks are thin, but have a high degree of continuity across the coating surface.

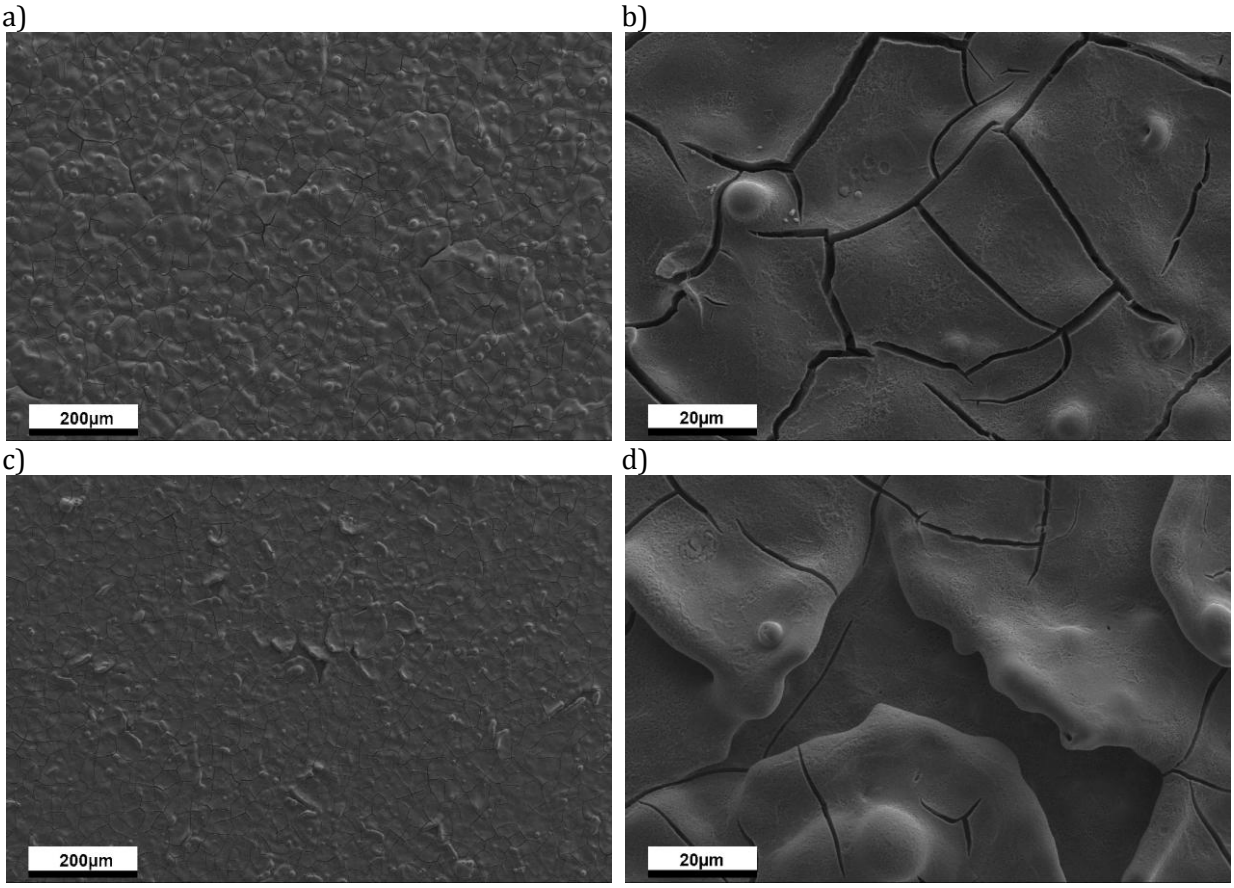

Figure 4.23: SEM micrographs of the surface microstructure for a) P-5-D.AR5.A5+5-D.A5 and b) P-2-D.AR5.A5+5-D.A5.

Cross section images of P-5-D.AR5.A5+5-D.A5 and P-2-D.AR5.A5+5-D.A5 (Figure 4.24) reveal a clear distinction between the applied layers. The top layers, only heat treated in air, possess the same lamellar structure characteristic for this heat treatment (Figure 4.11). In contrast, the bottom layers appear dense and similar to sample P-5-D.AR5+5-D.AR5.A5 and P-2-D.AR5+5-D.AR5.A5 (Figure 4.16). The thickness measured for P-5-D.AR5.A5+5-D.A5 range from 10-11 µm where each layer is between 5-6 µm. For P-2-D.AR5.A5+5-D.A5 the total thickness was found to be around 7 µm.

a) b)

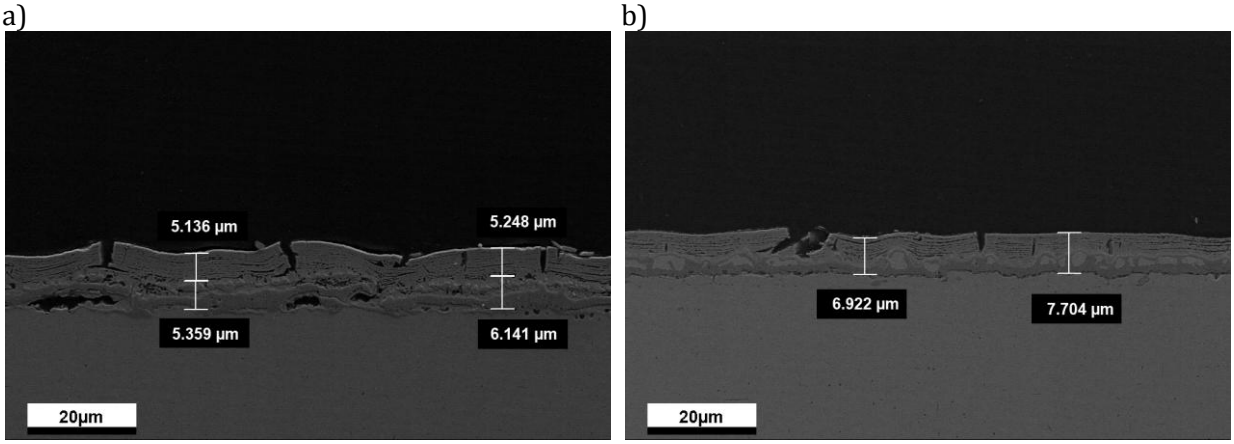

Figure 4.24: SEM micrographs of the cross section microstructure for a) P-5-D.AR5.A5+5-D.A5 and b) P-2-D.AR5.A5+5-D.A5.

In the case of the top layer, diffractograms of P-5-D.AR5.A5+5-D.A5 and P-2-D.AR5.A5+5-D.A5 (Figure 4.25) confirm that a phase pure top layer of $MnCo_2O_4$ was achieved for both samples. However, secondary phases remain in the bottom layers as illustrated by EDS-mapping of the cross sections (Figure 4.26).

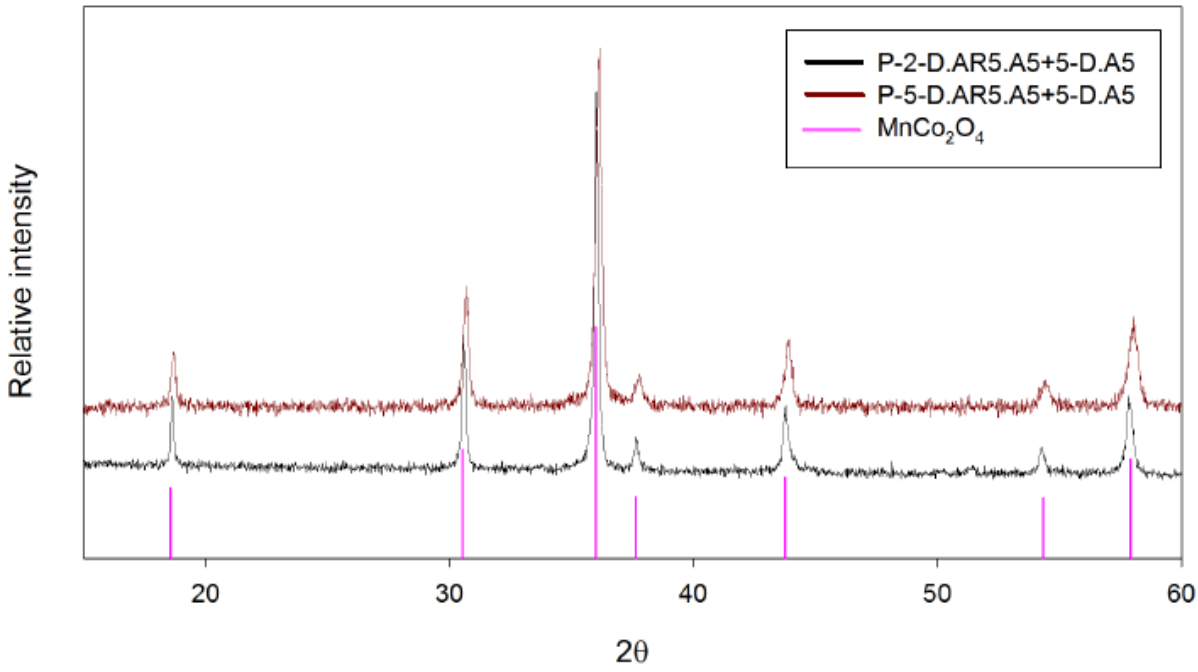

Figure 4.25: Diffractograms of P-5-D.AR5.A5+5-D.A5 and P-2-D.AR5.A5+5-D.A5.

Despite a phase pure top layer, elemental mapping of the P-2-D.AR5.A5+5-D.A5 coating surface reveals that chrome (in the form of chromia) is revealed through cracks in the top layer (Figure 4.27).

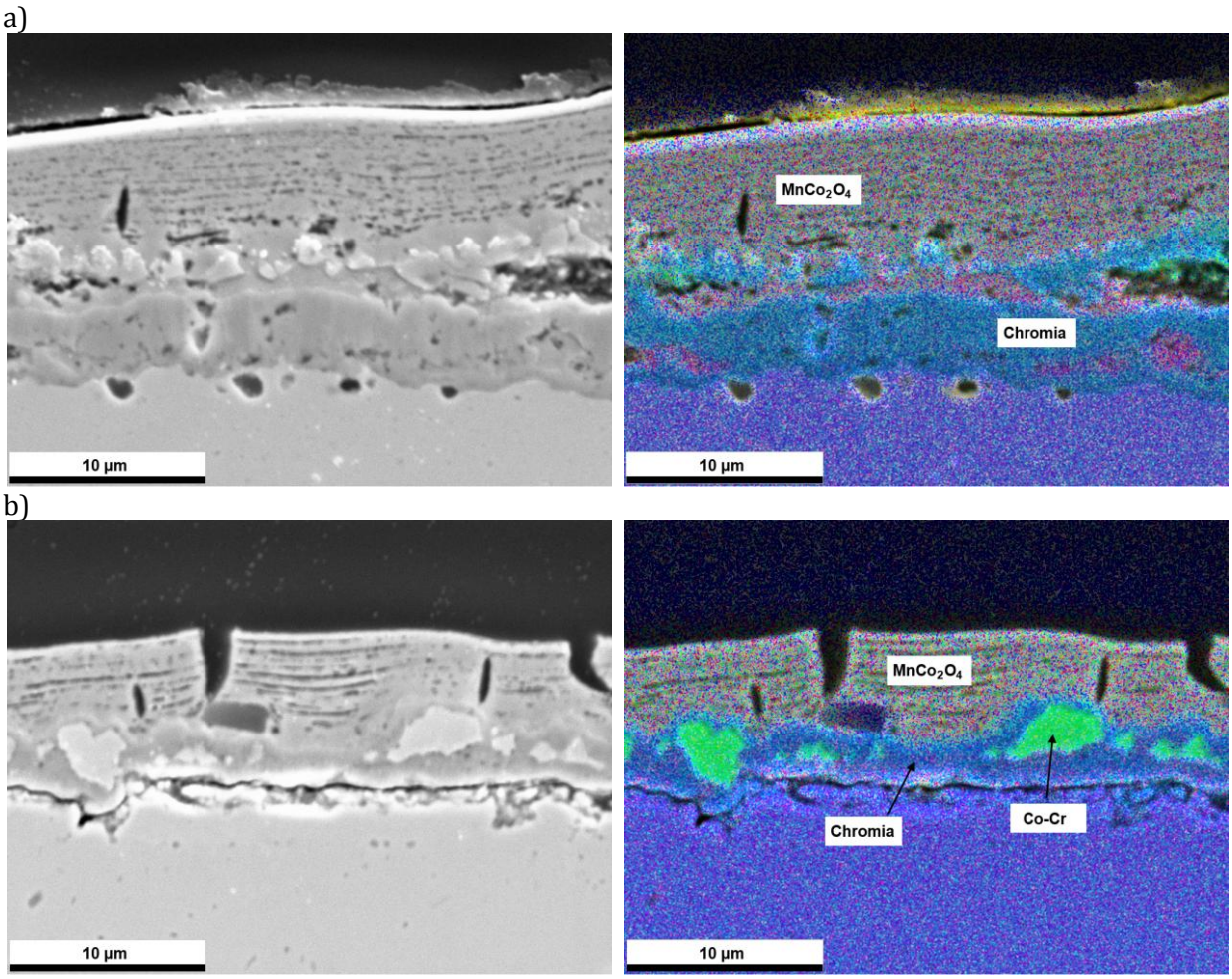

Figure 4.26: SEM image and EDS-map of a) P-5-D.AR5.A5+5-D.A5 and b) P-2-D.AR5.A5+5-D.A5.

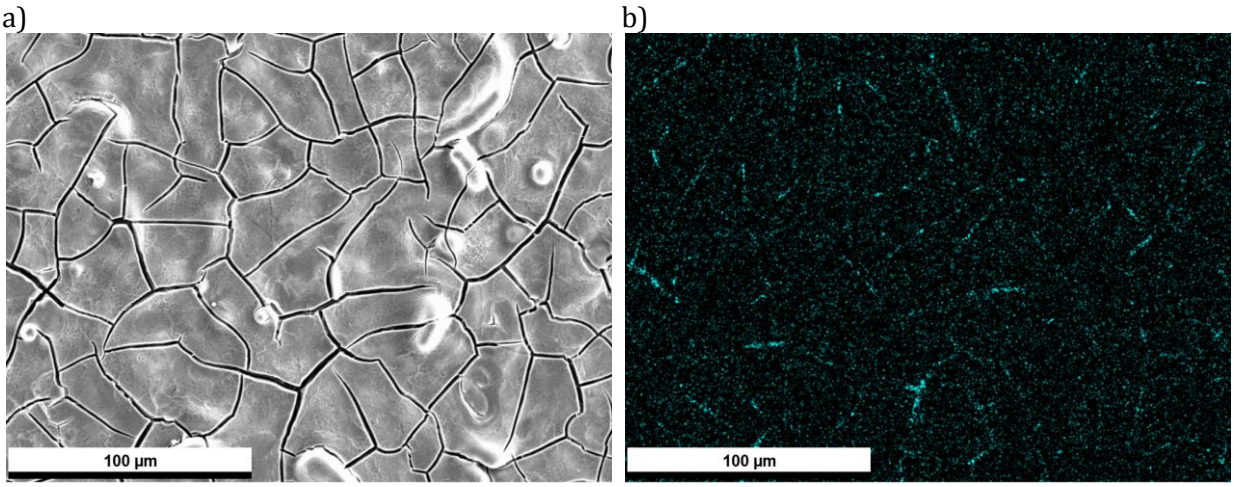

Figure 4.27: EDS map of P-2-D.AR5.A5+5-D.A5 surface. a) SEM image b) Cr-mapping

5 Discussion

5.1 Influence of substrate roughness

It is obvious that the substrate roughness has a major impact on the resultant coatings as seen in Figure 4.2 and Figure 4.3. Rougher substrates generate uneven coating thicknesses which generally are an unwanted trait and should be avoided. A good microstructure with few cracks may be futile, if a uniform thickness is not maintained. Additionally, further heat treatment of coatings applied on NA-substrates proved to induce stresses along the grooves and hills of the coating [10].

Regarding the grinded and polished substrates, crack evolution appeared more comprehensive for the coatings deposited on #500- and #800-substrates even as green coatings, but more notably as #800-5-D and #500-5-D. As for the NA-substrates, it is proposed that the inherent roughness of the substrates act as templates for crack growth. This is due to the morphology of rougher substrates, where coatings on certain areas such as grooves and hills are vulnerable to stresses. In turn, the stresses lead to crack evolution. Tensile stresses in particular should be avoided as ceramics are much more susceptible for these stresses. It is believed that tensile stresses manifest on top of the hills.

The situation is however reversed for the adhesion properties. As green coatings, only NA-5 displayed decent adhesion which is owed to its roughness, allowing mechanical anchoring of the coating layer. Accordingly, smoother substrates yield gradually inferior adhesion properties as demonstrated in the results. However, the fact that an exposure to 425 °C for 5 min significantly improved the coating adhesion, suggests that other adsorption forces – physical or chemical – are activated.

Since exposure to higher temperatures increased the adhesion properties, smooth, polished substrate surfaces were preferred for coating application. A polished substrate surface also mean that coatings will be less exposed to stresses as irregularities such as grooves and ridges are absent. Despite the fact that it is more difficult to process industrially, a uniform thickness, decent microstructure and apparently sufficient coating adhesion can be obtained. These factors improve the lifetime of the coatings which justify polishing the substrates.

5.2 Characterization of green coatings

Both the FTIR and TG results reveal that the green coating contains water and nitrate species. Decomposition of the nitrates occur around 150 °C and onwards, accelerating the crack growth as nitrogen gas is released from the coating. Furthermore, the mass loss does not end until 700 °C (for the selected heating rate). No matter, all prepared coatings must undergo heat treatments above this temperature in order to obtain the crystalline spinel oxide phase. As the operating temperature of the fuel cell is about 800

°C, a heat treatment in air should be above this temperature, but must be kept below 1000 °C as indicated by the phase diagram in Figure 2.2.

It is apparent that chemical reactions take place during heating. Evaporation of water and decomposition of nitrates has been mentioned and chromia can also form. In addition, the deposited film crystallizes to yield crystalline $MnCo_2O_4$. It is reasonable to believe that these reactions enhance the physical or chemical adsorption forces, thus improving the coating adhesion.

Another explanation for the weak adhesion of green coatings is owed to the highly hygroscopic ability of nitrates. Due to the water reabsorbed by the nitrate species after spray pyrolysis, the deposited film experiences a volume increase. As a result, the coating will delaminate to release the associated stresses [29]. However, the post-processed coatings, only exposed to 425 °C for 5 min, contradict this claim as they likely would still contain some nitrate species. That is not to say there is not a combination of these aspects. Nonetheless, the common factor points toward heat treatment as an essential process step to increase the adhesion.

5.3 Multilayered coatings

The initially prepared layers represented in Figure 4.6, support the assertion that heat treatments are necessary to obtain stable coatings that adhere well. This proved to be true for the primary layer as well as the final layer. Due to the horrendous result of sample P-5-D+5-D (Figure 4.6b), it was decided to spray a primary layer of 2 mL to see if the coating adhesion improved. At first glance sample P-2-D+5-D (Figure 4.6d), did indeed appear better, but no conclusive remarks could be made. Thus primary layers of both 5 mL and 2 mL were produced in order to further examine their effect on multilayered coatings.

5.3.1 Heat treatment in air

Exposure of the primary layer to 800 °C for minimum 2 h proved to be sufficient for a stable multilayer coating. However, the difference between 2 and 5 mL primary layers unravels when they are compared (Figure 4.8 and Figure 4.13). The general trend indicates that monolayers sprayed with 2 mL are smooth, whereas 5 mL layers exhibit more numerous and coarser cracks. This is explained by the fact that 2 mL coatings have a smaller volume to decompose, thus no extensive crack evolution occur.

The differences are carried on to their respective multilayer coatings. However, the situation seems to be reversed; multilayer coatings based on a 5 mL primary layer appear smoother compared to those based on a 2 mL bottom layer (Figure 4.10).

Also, it is worth mentioning that the crack features of 2 +5 mL coatings (Figure 4.7c-d and Figure 4.10c-d) are similar to that of the 5 mL monolayers (Figure 4.8a and Figure 4.13a).

An explanation of the differences between the multilayered coatings could be that the smooth 2 mL monolayers simulate the smooth surface of a polished substrate. Thus, the addition of a 5 mL layer will produce the same coating morphology as a 5 mL monolayer deposited on a polished substrate surface. On the other hand, a top layer added to a 5 mL primary layer will cover up the cracks and also adhere better to the coarse, rough crack openings as seen in Figure 4.10a and Figure 4.11a.

By evaluation of the cross sections, it becomes clear that heat treatments are necessary after application of each layer. Sample P-5-D.A2+5-D and P-2-D.A2+5-D in Figure 4.9a-c show that two deposited layers do not adhere to each other. In contrast, samples that have been heat treated both after deposition of the first and second layers appear as one thick layer. The additional heat treatment has in other words caused the two layers to sinter together. The degree of sintering and densification is also greater for the coatings subject to the heat treatment at 800 °C for five hours rather than two. This is well illustrated by the visibility of lamellar lines within the coating when comparing Figure 4.9b-d and Figure 4.11. The presence of lamellae is due to the slow spray rate of 0.3 mL/min which make the spraying discontinuous so it occurs as pulses on regularly intervals.

It is unsure whether or not the presence of lamellae deteriorates the overall coating properties as the lamellae run horizontally and provides no openings for the substrate to the surroundings. For poor lamellar structures, delamination might be of concern since the openings between the lamellae might increase and gradually loosen the lamellae. However, thin lamellar openings could be beneficial with respect to mitigation of vertical crack growth as they can dissipate the energy from the propagating cracks. Still, the porosity present between the lamellae will reduce the thermal conductivity and possibly the electrical conductivity as well. Thus, as a general guideline, coatings should be dense and form the basis for any coating considerations.

The thickest coating obtained of the samples discussed in this section, belongs to P-5-D.A5+5-D.A5 with a measured thickness of 8.374 µm. P-5-D.A5+5-D.A5 also exhibit the best adherence and coating microstructure. However, both the density and the crack features can be improved. As illustrated in Figure 4.12, the presence of cracks allows chrome from the substrate to be exposed to the surroundings, which deprive the coating of its primary function. Thus it is not ready for a commercial application.

Two solutions were proposed to improve the coating properties: 1) Heat treatment in argon in an attempt to densify and avoid unnecessary crack evolution. 2) Further application of a third layer to cover the previous cracks and also increase the thickness. Based on the ongoing work of Tobing et al. [38], heat treatments performed at 1100 °C for 5 h in argon was chosen for the continuation of the work

5.3.2 Heat treatment in argon

The idea of heat treatment in argon was to densify the coatings without using too high temperatures in air where the spinel phase would decompose. Also the absence of oxygen would prevent the formation of chromia.

The initial SEM images of the monolayers P-5-D.AR5 and P-2-D.AR5 (Figure 4.14) revealed neat coatings that were dense and crack free, as opposed to the samples processed in air. However, X-ray diffraction revealed that the integrity of the coating composition for either sample was not maintained (Figure 4.17a). The presence of $Mn_{1.45}Co_{1.55}O_4$ and phase impurities as CoO and Co_3O_4 imply that a heat treatment temperature of 1100 °C in argon yields a different phase equilibrium. A phase diagram for manganese cobalt oxide for oxygen partial pressures can be viewed in appendix B. The diagram can give an indication of the phase stability area, but for this experiment the oxygen partial pressure is not precisely known. It is believed to in the range of 10^{-7} Pa.

Nonetheless, Tobing et al. claim that phase pure coatings of $MnCo_2O_4$ were obtained by exposure to a second heat treatment in air at 800 °C for 5 h. This was not the case for the multilayered coatings P-5-D.AR5+5-D.AR5.A5 and P-2-D.AR5+5-D.AR5.A5 as shown by the diffractogram in Figure 4.17b. Admittedly, $MnCo_2O_4$, was detected, but so was Co_3O_4. According to the phase diagram (Figure 2.2), 800 °C corresponds to the single phase area of $MnCo_2O_4$. It was thought that the CoO would dissolve in a solid solution of $MnCo_2O_4$ at this temperature, but it appears that it oxidizes to Co_3O_4 during heating. According to the literature, this occurs at temperatures 390-800 °C [39]. As Co_3O_4 is stable at the heat treatment temperature, it cannot be removed.

Heating the coating to 900 °C would transform Co_3O_4 into CoO which should dissolve in solid solution at this temperature (Figure 2.2). However, the kinetics is unclear and any remaining CoO would re-oxidize into Co_3O_4 during cooling [10]. The presence of Co_3O_4 straight after heat treatment in argon thus suggests that the oxygen partial pressure was on a high enough level where oxidation of CoO was possible.

The findings in this study do however not contradict the results from Tobing et al. as their study of manganese cobalt coatings was based from a phase pure spinel powder, whereas this study starts from a precursor solution. The effects from the heat treatment are thus not directly transferable.

Application of a second layer heat treated only in air resulted in two layers with distinct differences. Yet, it appears that the manganese cobalt oxide layer adhere well to the chromia layer (Figure 4.24 and Figure 4.26). The good adhesion can be explained by the fact that $MnCo_2O_4$ and Cr_2O_3 have more similar features than $MnCo_2O_4$ and the FSS-substrate. Several studies now pre-oxidize the FSS-substrates before application of the interconnect coating in order to obtain a thin layer of Cr_2O_3 [40-42]. Nonetheless, cracks present in the top layer makes it easy for the chromium to volatilize from the chromia (Figure 4.27).

Due to the phase inhomoheneity of argon heat treated coatings, it is legitimate to say that on a general basis, heat treatment in argon at 1100 °C proved to be a failure since secondary phases such as CoO, Co_3O_4, Mn_2O_3 and Co-Cr were formed. In addition, the elevated temperature, prolonged and several heat treatments lead to the formation of Cr_2O_3 and $MnCr_2O_3$.

The fact that Cr_2O_3 is formed in an argon atmosphere considered non-oxidizing implies that the combination of a high heat treatment temperature and a relatively high oxygen partial pressure proved sufficient for chromia formation. In contrast, the lower heat treatment temperature of 800 °C in air did not yield any noticeable phase of Cr_2O_3.

By evaluation of the argon heat treatment from a positive perspective, a good surface microstructure was obtained, but this could be correlated to the secondary phases. The cross section microstructure was also admirable since they proved dense and free of lamellae which likely were caused by the elevated heat treatment temperature and longitude.

By consideration of the positive aspects of argon heat treatment, it might be worth investigating the phase stability conditions of $MnCo_2O_4$ in argon atmosphere. If the achieved microstructure turns out to be similar to those obtained at 1100 °C, outstanding coatings free of cracks may be achievable.

5.3.3 Coating thickness

The layer-by-layer approach was successful in terms of increasing the coating thickness. Maximum thickness registered for samples only heat treated in air was 8.374 µm (Figure 4.11a). Samples heat treated in argon had a thickness of 17.93 µm (Figure 4.16a) while samples with a primary layer heat treated in argon and a top layer only heat treated in air displayed a thickness of 11.39 µm (Figure 4.24a). However, the thickness value of 17.93 is inaccurate due to the voids in between the layers. Nonetheless, the thickness values are substantially higher when compared to monolayered coatings (Figure 4.3b).

Although the thickness is higher, it has to be questioned whether the coatings exposed to argon heat treatment has developed secondary phases that increase the overall coating thickness. The formation of a chromia or manganese chromium oxide layers by diffusion from the substrate is such an example. For a coating with an argon heat treated primary layer and a top layer heat treated only in air, Figure 4.24a and Figure 4.26a-b show that the chromia and $MnCo_2O_4$ layers each have a thickness of around 5 µm, giving a total coating thickness of 10 µm. For a multilayer coating only heat treated in air (Figure 4.11a) and that purely consists of $MnCo_2O_4$, the thickness of each layer would be around 4 µm, giving a total thickness of about 8 µm.

6 Conclusion

Coatings of $MnCo_2O_4$ have been deposited on the ferritic stainless steel, E-brite, by spray pyrolysis of an aqueous nitrate precursor solution. The influence of substrate surface roughness, layer-be-layer application and various heat treatments has been investigated in order to produce successful coatings with respect to density, thickness and crack features.

The study has demonstrated that substrates with higher surface finish yield the best coatings due to the resulting uniform thickness which leave the coating less susceptible for crack evolution. It was also shown that a heat treatment was necessary to obtain a decent coating adhesion.

Application of coatings with the layer-by-layer approach proved to be an efficient method to increase the overall coating thickness and at the same time heal cracks from the primary layer. The initial layers must however be subject to heat treatments before application of new layers. It was found that individual layers sprayed with a volume of 5 mL gave the best multilayer coatings in terms of the desired properties. Nevertheless, two layers of 5 mL heat treated in air, proved to be insufficient for successful coverage of the substrate due to the presence of vertical cracks that ran through both layers.

Heat treatments are found to be essential in order to achieve successful multilayered coatings. Higher temperature and longer treatment times yield denser coatings, but increase the probability of forming unwanted phases. For heat treatment in air, heating for 5 h at 800 °C is recommended. This ensures relative dense coatings with inconspicuous lamellae compared to a heating time of 2 h. Heat treatments in argon resulted in the best coating microstructure. Yet, a heating temperature of 1100 °C proved too high and caused the formation of secondary phases.

A maximum thickness of around 8 µm was found for a multilayered coating (two layers) heat treated in air. Multilayered coatings consisting of an argon heat treated primary layer and a top layer only heat treated in air, displayed a slightly higher thickness, albeit this is likely caused by the formation of a secondary phase, such as chromia, by diffusion from the surface.

7 Recommendations for further work

There are mainly two suggestions the author would like to point out for further work that is both related to two of the main goals in this study: thick and crack-free coatings.

Crack-free coatings were obtained for layers/coatings heat treated in argon although the phase purity was not maintained. Elucidation of the argon heat treatment is recommended in order to find an optimum heat treatment temperature where the phase purity is conserved, but still have the same crack-free microstructure that were obtained in this study.

The layer-by-layer approach successfully increased the thickness of the coatings. In addition, cracks from the primary layer appeared to be healed by the deposition of a second layer. However, this healing proved to be somewhat limited as it was shown that a number of cracks still ran through the whole coating cross section exposing chrome. Deposition of a third and even fourth layer could prove sufficient to heal all run-through cracks and at the same time increase the thickness. A more extensive layer-by-layer process should thus be of interest for any further work on this topic.

8 References

1. Stambouli, A.B. and E. Traversa, *Solid oxide fuel cells (SOFCs): a review of an environmentally clean and efficient source of energy.* Renewable & Sustainable Energy Reviews, 2002. **6**(5): p. 433-455.
2. Zhu, W.Z. and S.C. Deevi, *Development of interconnect materials for solid oxide fuel cells.* Materials Science and Engineering a-Structural Materials Properties Microstructure and Processing, 2003. **348**(1-2): p. 227-243.
3. Yang, Z.G., *Recent advances in metallic interconnects for solid oxide fuel cells.* International Materials Reviews, 2008. **53**(1): p. 39-54.
4. *Solid Oxide Fuel Celss (SOFCs)*. [cited 2013 20th April]; Available from: http://www.doitpoms.ac.uk/tlplib/fuel-cells/high_temp_sofc.php.
5. Yang, Z. and S.C. Singhal, *FUEL CELLS – SOLID OXIDE FUEL CELLS | Cell Interconnection*, in *Encyclopedia of Electrochemical Power Sources*, G. Editor-in-Chief: Jürgen, Editor. 2009, Elsevier: Amsterdam. p. 63-76.
6. Shaigan, N., et al., *A review of recent progress in coatings, surface modifications and alloy developments for solid oxide fuel cell ferritic stainless steel interconnects.* Journal of Power Sources, 2010. **195**(6): p. 1529-1542.
7. Xie, Y.S., et al., *Dense Protective Coatings for SOFC Interconnect Deposited by Spray Pyrolysis.* Fuel Cell Seminar 2009, 2010. **26**(1): p. 357-362.
8. Weber, S.B., *Spray Pyrolysis of Thermal Barrier Coatings*, 2012, Norwegian University of Science and Technology: Trondheim, Norway. p. 180.
9. Patil, P.S., *Versatility of chemical spray pyrolysis technique.* Materials Chemistry and Physics, 1999. **59**(3): p. 185-198.
10. Nguyen, T.X., *Project work: Spinel oxide protective coatings for solid oxide fuel cell interconnects*, 2012, NTNU: Trondheim, Norway.
11. Zhou, X.D. and S.C. Singhal, *FUEL CELLS – SOLID OXIDE FUEL CELLS | Overview*, in *Encyclopedia of Electrochemical Power Sources*, G. Editor-in-Chief: Jürgen, Editor. 2009, Elsevier: Amsterdam. p. 1-16.
12. Jeffrey, F. and Y. Zhenguo, *Interconnects*, in *Solid Oxide Fuel Cells*. 2008, CRC Press. p. 179-212.
13. Tucker, M.C., *Progress in metal-supported solid oxide fuel cells: A review.* Journal of Power Sources, 2010. **195**(15): p. 4570-4582.
14. Almeida, E., *Surface Treatments and Coatings for Metals. A General Overview. 1. Surface Treatments, Surface Preparation, and the Nature of Coatings.* Industrial & Engineering Chemistry Research, 2000. **40**(1): p. 3-14.
15. Allen, K.W., *"At forty cometh understanding": A review of some basics of adhesion over the past four decades.* International Journal of Adhesion and Adhesives, 2003. **23**(2): p. 87-93.
16. Bordeneuve, H., et al., *Cation distribution in manganese cobaltite spinels Co3−x Mn x O4 (0 ≤ x ≤ 1) determined by thermal analysis.* Journal of Thermal Analysis and Calorimetry, 2010. **101**(1): p. 137-142.

17. Yang, Z., et al., *(Mn,Co)3O4 spinel coatings on ferritic stainless steels for SOFC interconnect applications.* International Journal of Hydrogen Energy, 2007. **32**(16): p. 3648-3654.
18. Aukrust, E. and A. Muan, *Phase Relations in the System Cobalt Oxide–Manganese Oxide in Air.* Journal of the American Ceramic Society, 1963. **46**(10): p. 511-511.
19. Rios, E., et al., *Mixed valency spinel oxides of transition metals and electrocatalysis: case of the MnxCo3-xO4 system.* Electrochimica Acta, 1998. **44**(8-9): p. 1491-1497.
20. Wickham, D.G. and W.J. Croft, *Crystallographic and Magnetic Properties of Several Spinels Containing Trivalent Ja-1044 Manganese.* Journal of Physics and Chemistry of Solids, 1958. **7**(4): p. 351-360.
21. Bordeneuve, H., et al., *Structural variations and cation distributions in Mn3–xCoxO4 (0 <= x <= 3) dense ceramics using neutron diffraction data.* Solid State Sciences, 2010. **12**(3): p. 379-386.
22. Wu, J. and X. Liu, *Recent Development of SOFC Metallic Interconnect.* Journal of Materials Science & Technology, 2010. **26**(4): p. 293-305.
23. Fang, Y., et al., *High-temperature oxidation process analysis of MnCo2O4 coating on Fe–21Cr alloy.* International Journal of Hydrogen Energy, 2011. **36**(9): p. 5611-5616.
24. Yang, Z., et al., *Properties of (Mn,Co)3O4 Spinel Protection Layers for SOFC Interconnects*, in *Advances in Solid Oxide Fuel Cells II: Ceramic Engineering and Science Proceedings*. 2008, John Wiley & Sons, Inc. p. 231-240.
25. Chen, X., et al., *Protective coating on stainless steel interconnect for SOFCs: oxidation kinetics and electrical properties.* Solid State Ionics, 2005. **176**(5-6): p. 425-433.
26. Hua, B., et al., *The electrical property of MnCo2O4 and its application for SUS 430 metallic interconnect.* Chinese Science Bulletin, 2010. **55**(33): p. 3831-3837.
27. Petric, A. and H. Ling, *Electrical conductivity and thermal expansion of spinels at elevated temperatures.* Journal of the American Ceramic Society, 2007. **90**(5): p. 1515-1520.
28. Yang, Z., et al., *Development of (Mn,Co)3O4 Protection Layers for Ferritic Stainless Steel Interconnects*, 2005. p. Medium: ED; Size: PDFN.
29. Askestad, I., *Ceramic Thermal Barrier Coatings of Yttria Stabilized Zirconia Made by Spray Pyrolysis*, 2011, Norwegian University of Science and Technology: Trondheim, Norway.
30. Perednis, D. and L.J. Gauckler, *Thin film deposition using spray pyrolysis.* Journal of Electroceramics, 2005. **14**(2): p. 103-111.
31. Arca, E., K. Fleischer, and I.V. Shvets, *Influence of the Precursors and Chemical Composition of the Solution on the Properties of ZnO Thin Films Grown by Spray Pyrolysis.* Journal of Physical Chemistry C, 2009. **113**(50): p. 21074-21081.

32. Muecke, U.P., et al., *Initial stages of deposition and film formation during spray pyrolysis - Nickel oxide, cerium gadolinium oxide and mixtures thereof.* Thin Solid Films, 2009. **517**(5): p. 1522-1529.
33. Weber, S.B., et al., *Deposition Mechanisms of Thick Lanthanum Zirconate Coatings by Spray Pyrolysis.* Journal of the American Ceramic Society, 2011. **94**(12): p. 4256-4262.
34. *Technical Data Blue Sheet, Stainless Steel E-BRITE®.* [cited 2013 23rd May]; Available from: http://www.brownmetals.com/downloads/AlloyEbriteTechSheet.pdf.
35. Mayo, D.W., F.A. Miller, and R.W. Hannah, *Course notes on the interpretation of infrared and Raman spectra*. 2004: Wiley-Interscience.
36. Ion, E.D., et al., *Characterization of lanthanum zirconate prepared by a nitrate-modified alkoxide synthesis route: From sol to crystalline powder.* Journal of the European Ceramic Society, 2010. **30**(2): p. 569-575.
37. Mokkelbost, T., et al., *Combustion synthesis and characterization of nanocrystalline CeO2-based powders.* Chemistry of Materials, 2004. **16**(25): p. 5489-5494.
38. Tobing, S.L., *Deposition of manganese-cobalt oxide spinel on SOFC interconnect with electrophoresis system*, 2013, NTNU: Trondheim, Norway.
39. *Handbook of Preparative Inorganic Chemistry*. 1963, London: Academic Press Inc.
40. Hoyt, K.O., et al., *Oxidation behavior of (Co,Mn)3O4 coatings on preoxidized stainless steel for solid oxide fuel cell interconnects.* International Journal of Hydrogen Energy, 2012. **37**(1): p. 518-529.
41. Huang, K., P.Y. Hou, and J.B. Goodenough, *Characterization of iron-based alloy interconnects for reduced temperature solid oxide fuel cells.* Solid State Ionics, 2000. **129**(1–4): p. 237-250.
42. Ou, D.R., M. Cheng, and X.-L. Wang, *Development of low-temperature sintered Mn–Co spinel coatings on Fe–Cr ferritic alloys for solid oxide fuel cell interconnect applications.* Journal of Power Sources, 2013. **236**(0): p. 200-206.
43. Yankin, A.M. and V.F. Balakirev, *Phase Equilibria in the Co–Mn–Ti–O System over Wide Ranges of Temperatures and Oxygen Pressures.* Inorganic Materials, 2002. **38**(4): p. 309-319.

Appendix

A. Substrate surface microstructure

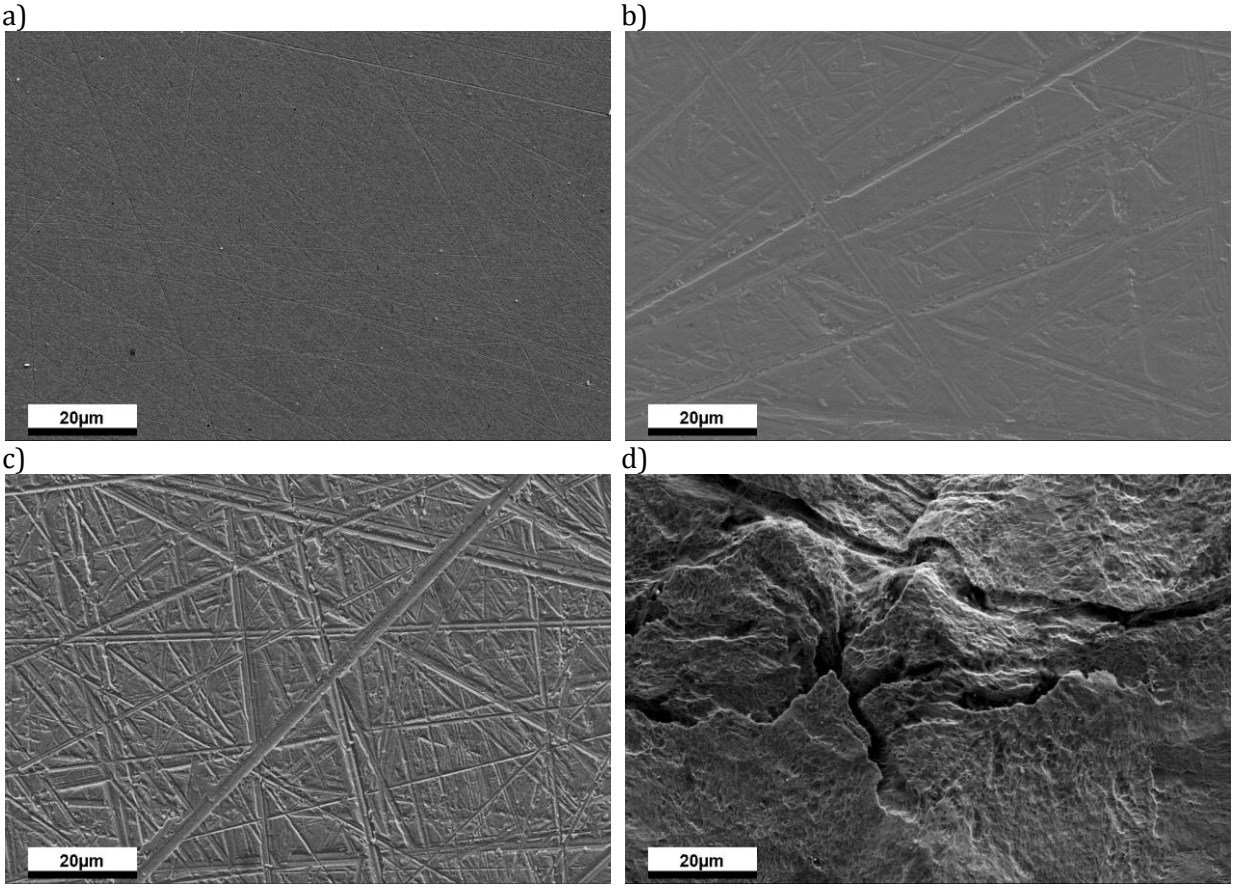

Figure A.1: SEM micrographs of the surface microstructure for a) P-substrate, b) #800-substrate, c) #500-substrate and d) NA-substrate. All substrates were cleaned in an acetone bath prior to image capture.

B. Phase diagram of manganese cobalt oxide with respect to partial oxygen pressure

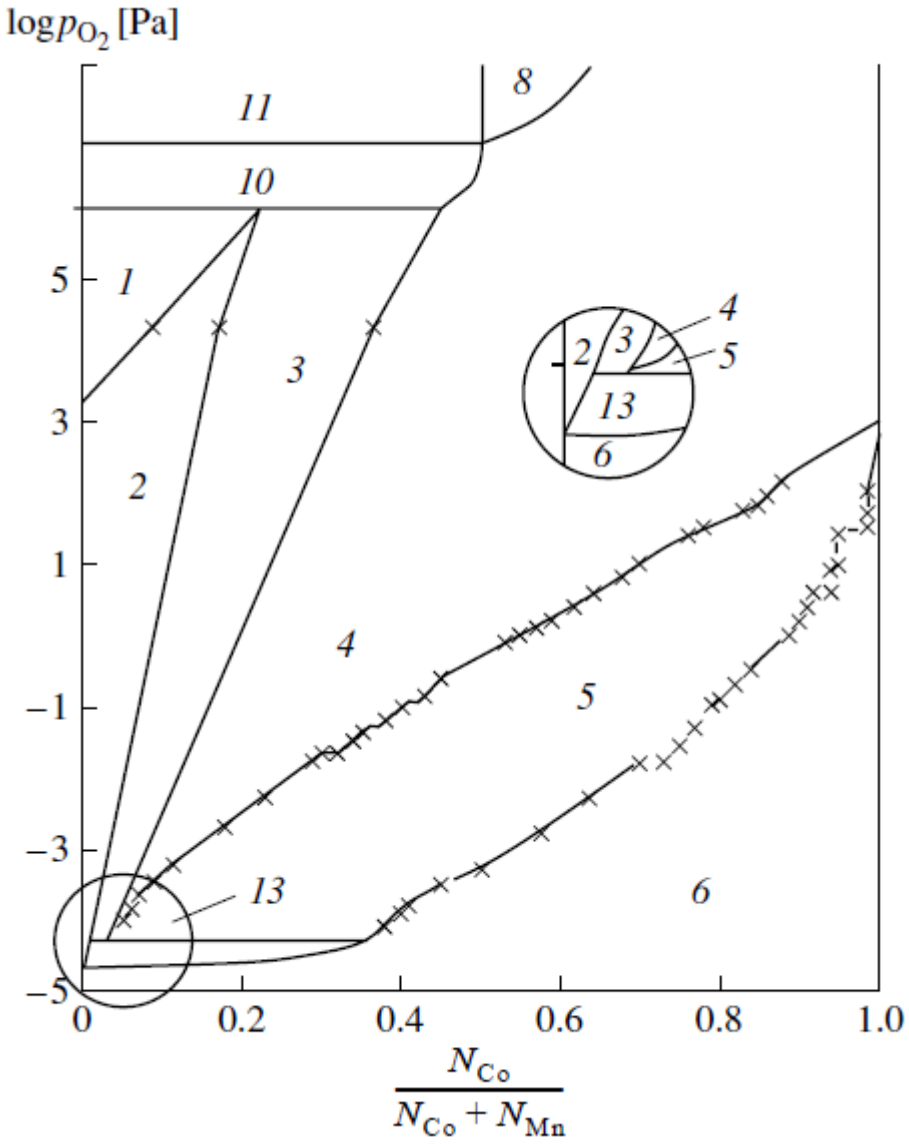

Figure B.1: 797 °C section of the Mn-Co-O system phase diagram for partial pressures of oxygen: (1) α-Mn_2O_3 + H. (2) H, (3) H + S, (4) S, (5) S + $Co_xMn_{1-x}O$, (6) $Co_xMn_{1-x}O$, (7) S + L, (8) L + $Co_xMn_{1-x}O$, (9) L, (10) S + α-Mn_2O_3, (11) α-Mn_2O_3 + $CoMnO_3$, (12) $CoMnO_3$ + S, (13) H + $Co_xMn_{1-x}O$ [43].